

THE NATURE OF FOSSIL GALAXY GROUPS: ARE THEY REALLY FOSSILS?

F. LA BARBERA¹, R. R. DE CARVALHO^{2,3}, I. G. DE LA ROSA⁴, G. SORRENTINO¹, R. R. GAL⁵, AND J. L. KOHL-MOREIRA⁶

¹ INAF-Osservatorio Astronomico di Capodimonte, Via Moiariello 16, 80131 Napoli, Italy

² VSTceN, via Moiariello 16, 80131 Napoli, Italy

³ Instituto Nacional de Pesquisas Espaciais/Divisão de Astrofísica Av. dos Astronautas 1758, São José dos Campos, SP, Brazil

⁴ Instituto de Astrofísica de Canarias, Tenerife, Spain

⁵ Institute for Astronomy, 2680 Woodlawn Dr., Honolulu, HI 96822, USA

⁶ Observatório Nacional, Rua General José Cristino 77, Rio de Janeiro, Brazil

Received 2008 June 9; accepted 2008 December 26; published 2009 March 10

ABSTRACT

We use SDSS-DR4 photometric and spectroscopic data out to redshift $z \sim 0.1$ combined with *ROSAT* All Sky Survey X-ray data to produce a sample of 25 fossil groups (FGs), defined as bound systems dominated by a single, luminous elliptical galaxy with extended X-ray emission. We examine possible biases introduced by varying the parameters used to define the sample, and the main pitfalls are also discussed. The spatial density of FGs, estimated via the V/V_{MAX} test, is $2.83 \times 10^{-6} h_{75}^3 \text{ Mpc}^{-3}$ for $L_X > 0.89 \times 10^{42} h_{75}^{-2} \text{ erg s}^{-1}$ consistent with Vikhlinin et al., who examined an X-ray overluminous elliptical galaxy sample (OLEG). We compare the general properties of FGs identified here with a sample of bright field ellipticals generated from the same data set. These two samples show no differences in the distribution of neighboring faint galaxy density excess, distance from the red sequence in the color–magnitude diagram, and structural parameters such as a_4 and internal color gradients. Furthermore, examination of stellar populations shows that our 25 FGs have similar ages, metallicities, and α -enhancement as the bright field ellipticals, undermining the idea that these systems represent fossils of a physical mechanism that occurred at high redshift. Our study reveals no difference between FGs and field ellipticals, suggesting that FGs might not be a distinct family of true fossils, but rather the final stage of mass assembly in the universe.

Key words: galaxies: clusters: general – galaxies: evolution – galaxies: formation – galaxies: fundamental parameters

Online-only material: color figures

1. INTRODUCTION

Searching for preserved remnants of physical processes that occurred in the cosmic past is one of cosmologists’ main tools in developing our understanding of how galaxies, groups, and clusters were formed and evolved, and ultimately came to define the large-scale structure we observe. Recent studies have shown that there seems to be a class of systems with exceptional preservation, known as fossil groups (FGs; Ponman et al. 1994). These systems consist of isolated, luminous early-type galaxies embedded in an extended X-ray halo. The main motivation for seeking such galactic systems stems from the fact that the merger timescales for $L > L^*$ group galaxies is much shorter than the cooling timescales for the hot gas component within which these bright galaxies are embedded (e.g., Barnes 1989; Ponman & Bertram 1993). In this simplistic view, FGs are a natural consequence of the merging process in normal groups and therefore can be used to trace the history of coalescence in the not-so-high-redshift universe.

From the observational viewpoint, FGs are seen in the optical as large elliptical galaxies, but with X-ray luminosities comparable to those of an entire group of galaxies ($L_X > 4.4 \times 10^{42} \text{ erg s}^{-1}$; see Jones et al. 2003, hereafter JO03). To date, no clear picture of their origin has emerged from the collected data. Two main scenarios have been suggested: FGs result from the complete merging of galaxies that constituted a loose group in the past, collapsing at an early epoch, but never becoming incorporated into clusters (Hausman & Ostriker 1978; Ponman et al. 1994; Jones et al. 2000; Khosroshahi et al. 2004); or they originate from a region that inhibits formation of L^*

galaxies in these groups leading to an atypical galaxy luminosity function (LF; Mulchaey & Zabludoff 1999).

These systems have been detected out to redshifts of at least $z \sim 0.6$ (Ulmer et al. 2005), have high M/L ratios suggesting low star formation efficiency (Vikhlinin et al. 1999), and represent 8%–20% of all systems with similar X-ray luminosities. Ten FGs are already known and well studied from optical and X-ray data (Mulchaey & Zabludoff 1999; Romer et al. 2000, hereafter R00; Jones et al. 2003; Khosroshahi et al. 2004; Sun et al. 2004; Yoshioka et al. 2004; Ulmer et al. 2005). A recent paper by Santos et al. (2007) presents a sample of 34 FG candidates based on Sloan Digital Sky Survey (SDSS) data. In this work, we use optical (SDSS) and X-ray (*ROSAT* All Sky Survey—RASS) data to define a sample of FG candidates. We select FGs following a strategy similar to Jones et al. (2003), using spectroscopic (age, metallicity, α/Fe enhancement) and photometric (a_4 , color gradient) parameters to further constrain what should be an FG. The main goal is to establish a link between FGs, compact groups, and isolated ellipticals based on their global properties and simple expectations, if mergers are the dominant events determining the evolution of a FG.

This paper is organized as follows. Section 2 presents the galaxy catalog used to search for FGs, describing the parameters and the X-ray measurements that define the search. The actual selection of FGs is then detailed. Section 3 presents the control sample used to compare FG properties to those of “normal” ellipticals, which in principle did not result from merging. Section 4 discusses the magnitude distribution of the brightest and second brightest galaxies of FGs, while in Section 5 we characterize the distribution of the faint galaxies around FGs.

Since FGs are thought to be old systems, in Section 6 we examine the colors of FGs relative to the red sequence of early-type galaxies. Section 7 deals with the internal structure of seed galaxies of FGs, as measured by their structural parameters and internal color gradients. In Section 8, we analyze stellar population properties of FGs, by looking at the distributions of age, metallicity, and α enhancement. Finally, in Section 9, we summarize and discuss the main results. Throughout the paper we use a cosmology with $\Omega_m = 0.3$, $\Omega_\Lambda = 0.7$, and $H_0 = 75 \text{ km s}^{-1} \text{ Mpc}^{-1}$.

2. SELECTION OF FGS

FGs are defined as bound systems of galaxies associated with extended X-ray sources. The total optical luminosity of these systems is dominated by a bright elliptical galaxy, and their LF exhibits a gap between the first and second-rank galaxies (see e.g., Jones et al. 2003). The sample of FG candidates defined here is selected on the basis of spectroscopic and photometric data from the Data Release 4 (DR4) of the SDSS, and on the basis of RASS X-ray imaging. The optical selection is described in Section 2.1, while the X-ray measurements and the definition of the FG sample are presented in Section 2.2.

2.1. The SDSS Catalog and the Optical Selection Parameters

The optical selection is performed on a complete volume-limited catalog of 91563 galaxies, retrieved from the SDSS-DR4 database⁷ through the CasJobs facility⁸. The catalog consists of all galaxies with absolute r -band magnitudes M_r brighter than -20 and with spectroscopic redshifts between 0.05 and 0.095 . Absolute magnitudes are obtained from the SDSS r -band Petrosian magnitudes, corrected for galactic extinction using the reddening maps of Schlegel et al. (1998). The lower redshift limit of the catalog is chosen to minimize the aperture bias (Gómez et al. 2003), which strongly affects large nearby galaxies, while the upper redshift limit guarantees a high level of completeness, estimated through Schmidt's V/V_{max} test (see Sorrentino et al. 2006). The magnitude limit of -20 corresponds approximately to the apparent magnitude limit of the SDSS spectroscopy at redshift $z \sim 0.095$ ($r \sim 17.8$).

Since FGs are systems characterized by a gap in the galaxy LF, we first select optical candidates by searching the SDSS spectroscopic database for pairs of galaxies whose magnitude difference is larger than a given value, ΔM_{min} . For each galaxy in the catalog, we select all objects whose projected distance on the sky from the target galaxy is smaller than a maximum radius, D_{max} , and whose redshift difference is smaller than a given value, $\Delta(cz_{\text{max}})$. In other words, for each galaxy, we select companion galaxies in a cylinder centered on the galaxy, with a radius of D_{max} and a semiheight of $\Delta(cz_{\text{max}})$ along the line of sight. The value of D_{max} is fixed in physical units (Mpc), and the selection is done by transforming the value of D_{max} to the apparent size that corresponds to the redshift of the seed galaxy. A bright galaxy is defined as a possible FG if (1) there is at least one companion selected through the above procedure, and (2) if all the companions are fainter, with the magnitude difference greater than ΔM_{min} . Thus, our optical FG candidates are selected on the basis of three parameters: $\Delta(cz_{\text{max}})$, D_{max} , and ΔM_{min} . The parameters $\Delta(cz_{\text{max}})$ and D_{max} are used to select the companions of a given galaxy in the SDSS catalog, while

the parameter ΔM_{min} characterizes the gap in the LF between the galaxy and its companions.

To determine suitable values of $\Delta(cz_{\text{max}})$, D_{max} and ΔM_{min} , we examine how the number of optical FG candidates and the corresponding contamination rate change as a function of these parameters. The parameters are chosen in such a way that the contamination rate is at most 15%, defined as the fraction of FG candidates that would be selected (for a given set of values of $\Delta(cz_{\text{max}})$, D_{max} and ΔM_{min}) from a random distribution of galaxies with the same mean galaxy surface density, magnitude, and redshift distributions as the SDSS catalog. We generated randomized galaxy catalogs by applying the shuffling method, as described in Gal et al. (2003). First, we bin the SDSS catalog in 4° in right ascension and declination, and $\Delta z = 0.005$ in redshift. The randomized catalog is then obtained by shuffling galaxies in each bin by randomly exchanging their right ascension, declination, and redshift. The above bin sizes are chosen such that both the mean surface density and the redshift distribution of galaxies in the SDSS catalog are preserved, without overly reducing the number of galaxies in each bin. We verified that varying these bin sizes by 20% does not change the contamination rate estimates. Figure 1 compares the characteristics of the galaxy catalog with those of one of the shuffled catalogs. The shuffled catalogs reproduce well the sky coverage of the SDSS-DR4 catalog as well as the corresponding distributions of galaxy magnitudes and redshifts. Since the shuffling procedure washes out small scale structures from the galaxy catalog, the FG candidates that are selected from the shuffled catalogs only arise as rare and random instances in the magnitude, redshift, and spatial distributions of the galaxies, instead of a population of objects that follow from some physical evolutionary path. To reduce statistical fluctuations in the contamination rate estimates, we repeat the shuffling procedure 100 times and estimate the contamination rate as the ratio of the number of optical FG candidates to the mean number of candidates selected from the shuffled catalogs applying the same $\Delta(cz_{\text{max}})$, D_{max} , and ΔM_{min} criteria.

Figures 2 and 3 show the number of FG optical candidates and the contamination rate as functions of $\Delta(cz_{\text{max}})$, D_{max} and ΔM_{min} . We vary $\Delta(cz_{\text{max}})$ from 0.00025 ($\sim 75 \text{ km s}^{-1}$), corresponding to ~ 2.5 times the typical redshift uncertainty of the SDSS spectroscopic sample,⁹ to 0.0065 , corresponding to $\sim 2000 \text{ km s}^{-1}$, i.e., about 2 times the typical velocity dispersion of a rich cluster of galaxies. The minimum value of D_{max} is chosen to be 0.3 Mpc , which is about twice the typical core radius of galaxy clusters (Adami et al. 1998). Furthermore, we consider only values of D_{max} smaller than 0.6 Mpc , since higher values yield contamination rates greater than $\sim 20\%$ for all possible values of the other two parameters. Finally, we consider only values of ΔM_{min} in the range of 1.5 – 2.5 mag . The value of 1.5 is chosen to have a reasonable minimum gap in the LF of FG candidates, while values of ΔM_{min} larger than 2.5 are excluded since they overly reduce the number of candidates. Looking at Figure 2, we see that the number of candidates shows a maximum at $\Delta(cz_{\text{max}}) \sim 0.001$ for a wide range of values of both D_{max} and ΔM_{min} . Hence, to maximize the sample size, we adopt this value of $\Delta(cz_{\text{max}})$. For D_{max} , we see that for fixed values of $\Delta(cz_{\text{max}})$ and ΔM_{min} the number of candidates does not change significantly for $0.35 \lesssim D_{\text{max}} \lesssim 0.5 \text{ Mpc}$. On the other hand, the contamination rate changes by a factor of 2

⁷ <http://www.sdss.org/DR4>

⁸ <http://casjobs.sdss.org/casjobs/>

⁹ For the SDSS-DR4 main galaxy sample, the typical redshift accuracy is 30 km s^{-1} (see <http://www.sdss.org/dr4/>).

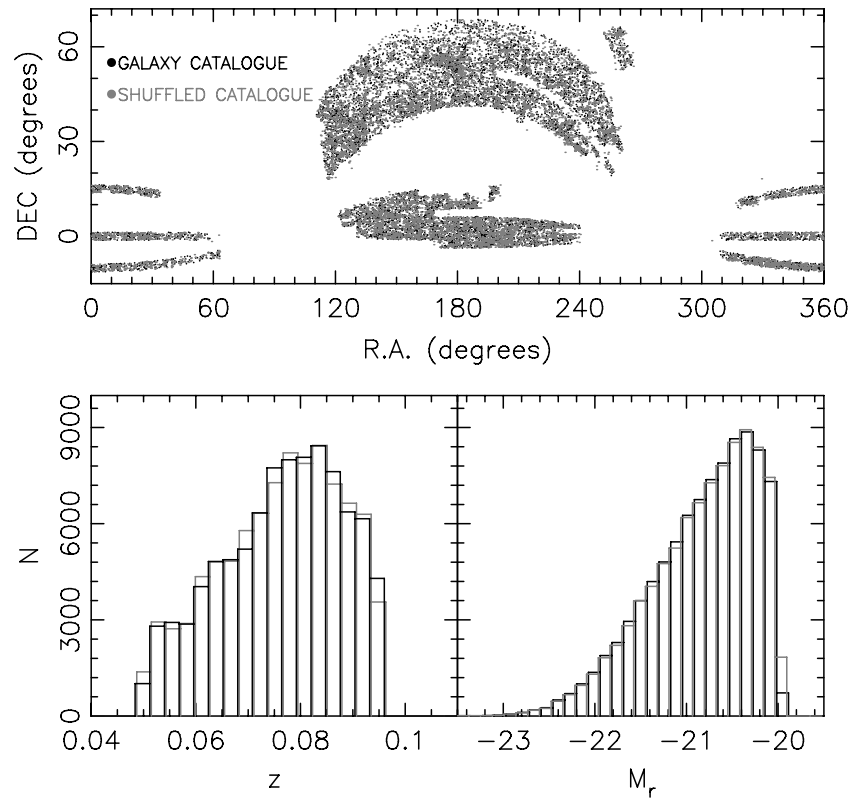


Figure 1. Comparison of the characteristics of the galaxy catalog with those of one of the shuffled catalogs. The upper panel plots declination vs. right ascension and compares the sky area covered from both catalogs. The lower left and right panels show the redshift and magnitude distributions, respectively, of galaxies in both catalogs. As shown in the upper panel, galaxies from the shuffled and the galaxy catalogs are plotted with gray and black colors, respectively.

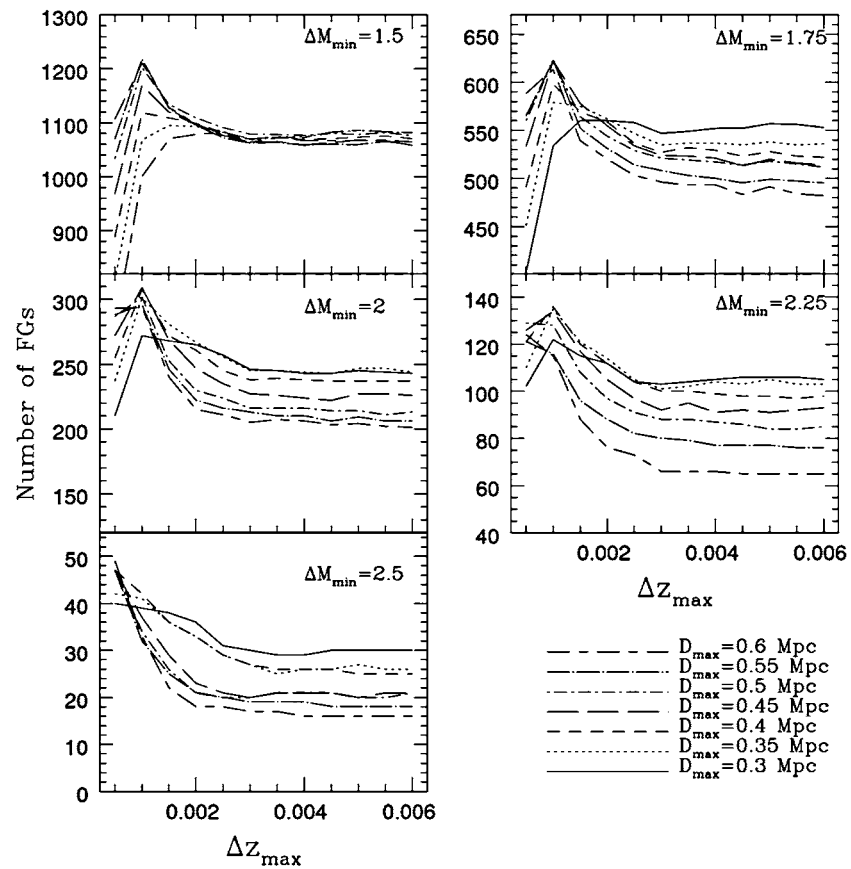


Figure 2. Number of FG candidates as a function of the selection parameter Δz_{\max} . The panels correspond to different values of ΔM_{\min} (shown in the upper right of each plot), while different line styles correspond to different values of D_{\max} , as shown in the lower right corner of the figure.

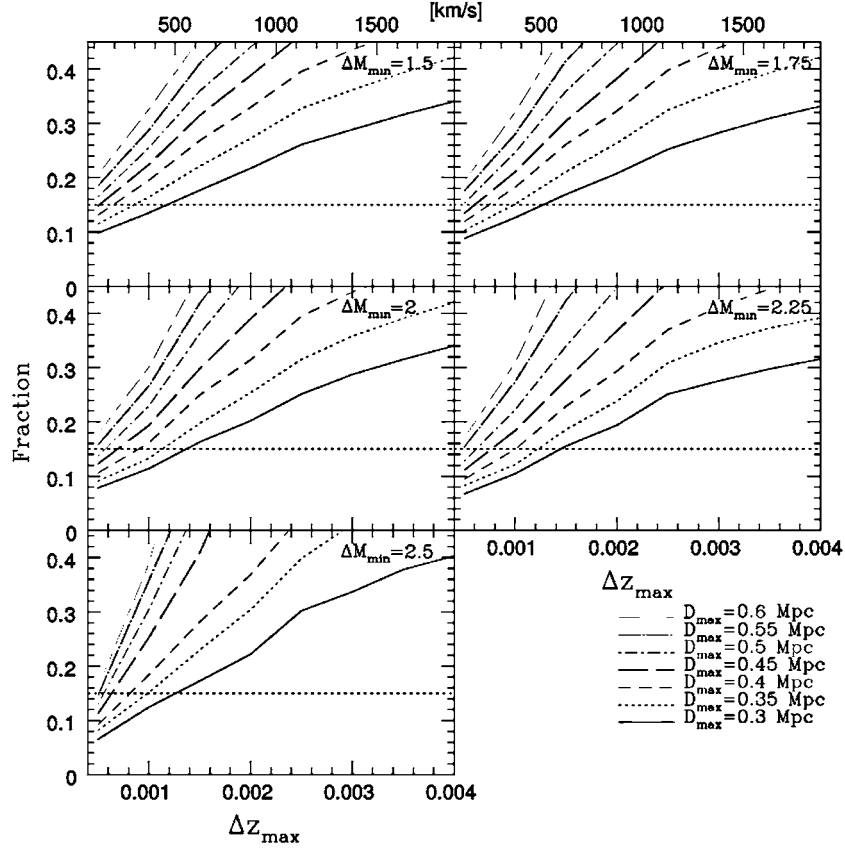


Figure 3. Same as Figure 2 but showing the corresponding contamination rates as estimated through the shuffling method (see the text). In each panel, the dotted horizontal line marks the upper limit for the acceptable level of contamination in the sample of FG candidates.

over the full range of values of D_{\max} . We choose a suitable value of D_{\max} by fixing an upper limit to the contamination rate. Examining Figure 3 and considering all the values of ΔM_{\min} which correspond to $\Delta(cz_{\max}) = 0.001$, contamination rates less than 15% are achieved only for $D_{\max} \lesssim 0.35$ Mpc. Since the number of FG candidates decreases as a function of D_{\max} , we adopt $D_{\max} = 0.35$ Mpc. Finally, we have to determine the choice of ΔM_{\min} . Figure 4 plots the contamination rate as a function of ΔM_{\min} for all possible values of D_{\max} and $\Delta(cz_{\max})$. We see that the contamination is almost constant for $\Delta M_{\min} \lesssim 2.2$, with an increase for larger values of ΔM_{\min} . Figure 5 plots the number of FG candidates as a function of ΔM_{\min} for $\Delta(cz_{\max}) = 0.001$ and $D_{\max} = 0.35$ Mpc. The number of FG candidates rapidly decreases as ΔM_{\min} increases, reaching almost 0 at $\Delta M_{\min} \sim 2.5$. In order to obtain a statistically significant number of FG candidates without overly reducing the ΔM_{\min} gap, we decided to adopt $\Delta M_{\min} = 1.75$ mag.

To summarize, the values of the three parameters $\Delta(cz_{\max})$, D_{\max} and ΔM_{\min} are chosen as a compromise between the number of selected FG candidates and the corresponding contamination rates. We adopt the following parameters: $\Delta(cz_{\max}) = 0.001$, $D_{\max} = 0.35$ Mpc, and $\Delta M_{\min} = 1.75$ mag, resulting in a list of 578 optical FG candidates. Note that the D_{\max} value is close to half of the virial radius ($0.37 h_{75}^{-1}$ Mpc) assuming a temperature of 1 KeV and the mean redshift of the sample (Evrard et al. 1996). As found by Khosroshahi et al. (2007), based on *Chandra* data, a typical temperature for FGs is 1 KeV, with a few systems having a temperature as high as ~ 3 KeV. In the latter case, half the virial radius is 0.64 Mpc. Using such a large D_{\max} results in a high contamination rate for whatever value of $\Delta(cz_{\max})$ and ΔM_{\min} (see Figure 4).

We note that the above selection of FG systems can be affected by the SDSS spectroscopic incompleteness, because of the SDSS fiber collision limit preventing neighboring fibers from being closer than $55''$. This prevents complete spectroscopic coverage of objects in dense regions, even in cases where multiple tiles overlap. It is therefore, possible to have galaxies adjacent to some optical FG candidates which would nominally disqualify them, but lacking SDSS spectroscopy, the neighbors would not be taken into account by our selection procedure. This issue is addressed in Section 2.2.2.

2.2. X-Ray Analysis and the Final Sample of FGs

2.2.1. Measuring X-Ray Fluxes with RASS

The X-ray luminosity L_X of each optical FG candidate is estimated using RASS countrates.¹⁰ The first step is to estimate the background contribution, by randomly selecting 100 boxes each with an area of 100 square arcmin, located throughout the 6.5×6.5 field containing the target, and then taking the median and the rms of these 100 values. The count rates are integrated in three apertures, with radii of 5, 10, and 20 times the effective radius, r_e , of the FG seed galaxies. Effective radii are measured from the *r*-band SDSS images, as described in Appendix C. We considered a detection as significant when the S/N is at least 3σ above the background, otherwise we derive upper limits as in Beuing et al. (1999). We selected for further analysis only those systems with a significant X-ray detection in at least one of the three measured apertures, resulting in a sample of 113 (out of 578) FG candidates.

¹⁰ <ftp://ftp.xray.mpe.mpg.de/rosat/archive/900000>

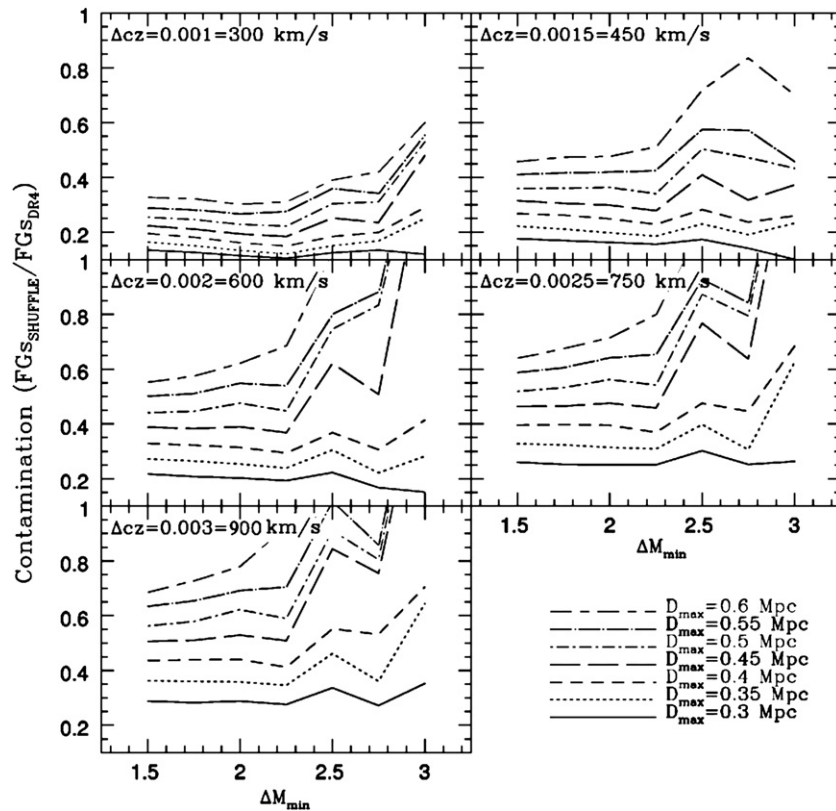


Figure 4. Contamination rate as a function of ΔM_{\min} . Each plot corresponds to a different value of $\Delta(cz_{\max})$, as shown in the upper right of each panel. Curves with different line styles correspond to different values of D_{\max} , and are the same as in Figure 2.

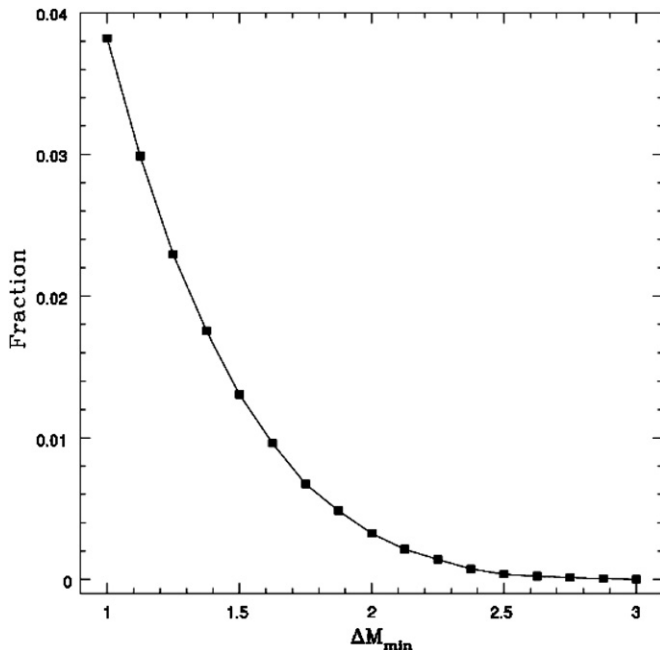


Figure 5. Fraction of FG candidates in the SDSS catalog as a function of ΔM_{\min} for the values of $D_{\max} = 0.35$ Mpc and $\Delta(cz_{\max}) = 0.001$ adopted to select FG candidates. The black curve is obtained from a cubic interpolation of the data.

To convert the measured total count rate into an unabsorbed X-ray flux in the *ROSAT* 0.5–2.0 keV energy band, we use the HEASARC PIMMS tool. We assume a Raymond–Smith spectrum to represent the hot plasma present in the intracluster

medium (Raymond & Smith 1977) with solar metallicity and an interstellar hydrogen column density along the line of sight given by Bajaja et al. (2005). The plasma temperature is fixed at 1 keV, which is typical for very bright elliptical galaxies (Beuing et al. 1999), although the dependence of the flux on the temperature used is insignificant (less than 5%). Finally, the rest frame 0.5–2.0 keV flux was obtained by applying the k -correction as in Böhringer et al. (2000).

2.2.2. Contamination by Spirals, AGN, and Clusters

To refine the selection of FGs, we considered four possible sources of contamination: (1) spiral galaxies; (2) active galactic nucleus (AGN); and (3) superpositions with rich clusters of galaxies.

1. Since FGs are dominated by a bright elliptical galaxy, we removed contaminating spiral galaxies from the list of optical candidates. We fit the SDSS r -band image of each galaxy with a seeing convolved Sersic model (see Appendix C for details), and flagged as spirals those objects with a detectable spiral arm pattern in the residual map obtained after model subtraction. This procedure eliminates 91 (out of 578) contaminating systems.
2. We flagged those FG optical candidates with AGN spectral signatures and excluded them from the analysis. AGNs were selected following the criteria described in Sorrentino et al. (2006). We removed 45 (out of 578) galaxies.
3. The above selections leave a sample of 102 FG candidates with significant X-ray detections, no significant AGN signatures, and early-type morphology.
4. The resolution and S/N of RASS is insufficient to differentiate between X-ray emission from a real FG and that

from a rich cluster which happens to be along the line of sight. Moreover, for a rich cluster, the SDSS spectroscopic incompleteness at the bright end might mimic the lack of bright companion galaxies required to be an FG. Thus, we rejected FG candidates within 1.5 Mpc (at the FG redshift) from a rich Abell cluster. We discarded $R > 0$ Abell clusters with the exception of Abell 690 (richness $R = 1$; FG 22 of Table 2), for which we verified that there are no galaxies with available photometry from SDSS that might invalidate our adopted fossilness definition. 28 (out of 102) FG candidates were discarded with this criterion, leaving a sample of 74 FG candidates.

Although we eliminated AGN and spiral galaxies from the sample, we further investigated the presence of elusive emission lines in the SDSS spectra of the 102 FGs with significant X-ray detections. For each spectrum, we modeled the absorption lines with a combination of stellar-population models using the STARLIGHT code (Cid Fernandes et al. 2005). Further details of the procedure are presented in Section 8. After subtracting the old stellar component, we measured the remaining O_I , O_{II} , O_{III} , H_α , H_β , and N_{II} emission features. Figure 6 displays the diagnostic diagrams defined with these indices. Regions corresponding to different types of active galaxies are plotted according to the definition of Kewley et al. (2006). Only nine FG candidates have residual emission lines typical of AGN. In agreement with expectations from our morphological selection, no starburst galaxies (H II) are found in the FG sample. Moreover, almost all of the AGN are classified as LINERs, which have a typical X-ray luminosity of 10^{40} erg s $^{-1}$ (see Komossa et al. 1999), 2 orders of magnitudes lower than the minimum X-ray luminosity of the FGs in our sample. Thus, we conclude that AGN and starburst contamination does not contribute significantly to the X-ray measurements, except for AGN that might be detected only in X-rays. However, as noted by Anderson et al. (2007), these account for only a minor fraction of all AGN.

2.2.3. How Extended is the X-Ray Emission?

An important issue to consider is whether the observed X-ray luminosity comes from an extended source. Although AGN were excised from our sample following the recipes in Sorrentino et al. (2006), some AGN might only be detected in X-ray (Tozzi et al. 2006; Anderson et al. 2007), representing further a source of contamination in the FG sample. To objectively establish the extended nature of the X-ray emission we proceed as follows:

1. We select 1232 point sources from the RASS Bright Source Catalog (Voges et al. 1999), requiring that the sources have a high probability of being a real detection (i.e., source detection likelihood greater than 100) and a source extension of zero. This data set was used to measure the mean FWHM of the RASS point-spread function (PSF) over the whole sky. We used 2DPHOT (La Barbera et al. 2008) to fit a Moffat distribution to every source, after a Gaussian smoothing (with a σ of 1 pixel) of the original count-rate image. The smoothing was done similarly for the FGs (see below). Figure 7 shows the distribution of the FWHM for the 1232 point sources. The location of the peak of the distribution (and its error) was obtained from the biweight estimator (Beers et al. 1990) and is found to be $2.66(\pm 0.02)$ arcmin. The narrowness of the distribution

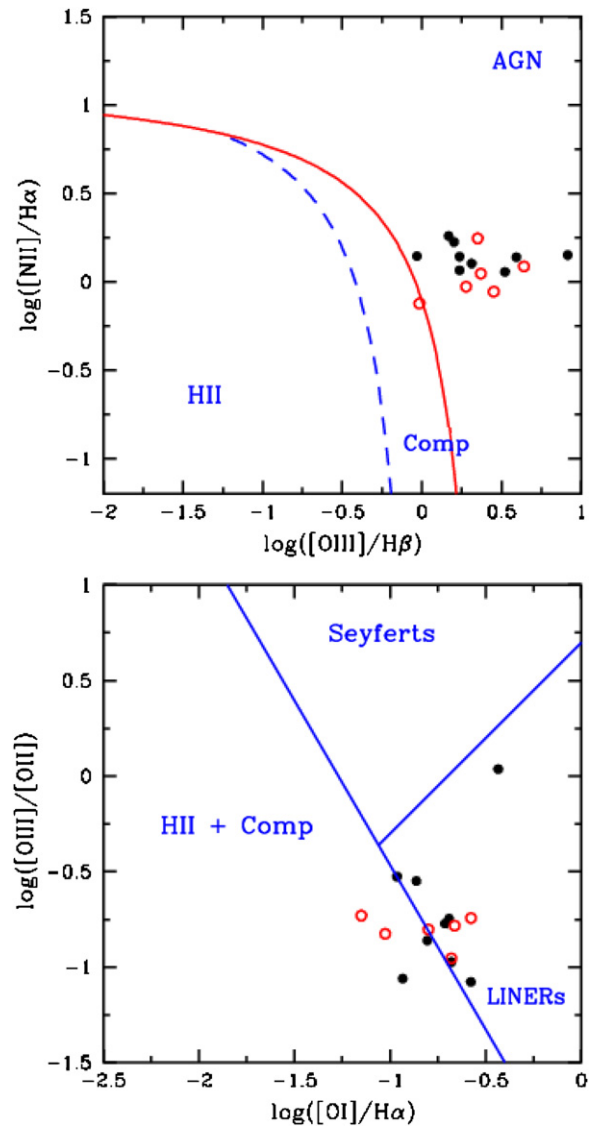


Figure 6. Diagnostic diagrams showing the nine FG candidates (filled circles) which still show some emission lines in the SDSS spectra. The empty circles represent the six field galaxies (FS; see Section 3) with some residual emission features in the SDSS spectra. We also display the regions defining the locus for AGN (Seyfert and LINERs) and starbursts (H II). Notice that the figure also shows the transition region between AGN and H II.

(A color version of this figure is available in the online journal.)

confirms the expectations that the RASS PSF has little off-axis variation resulting from the scanning strategy. We also verified that fitting the unsmoothed images gives a mean FWHM of 2.15 arcmin, in good agreement with the value of 2.1 arcmin from de Grandi et al. (1997).

2. For the 74 FGs, we smoothed the original RASS images with a 1 pixel Gaussian (as for the point sources). Source detection was performed using SExtractor with a detection threshold of 2σ over an area of 5 pixels, using a tophat detection filter, which is optimal for faint source detection. The Gaussian smoothing enhances the contrast over the background. For each FG, we identified the closest X-ray source to the SDSS position.
3. Using the smoothed X-ray images, we fit a Moffat distribution to the FG candidates. Here, the error in the FWHM was estimated from 100 Monte Carlo simulations. For each

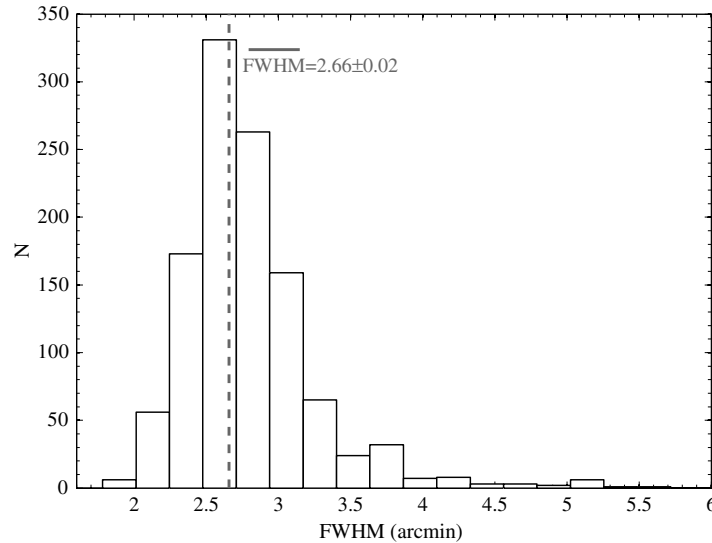


Figure 7. Distribution of FWHM values for 1232 point sources in the RASS Bright Source Catalog. The vertical dashed line marks the position of the peak of the distribution. The location of the peak, $FWHM$, and the corresponding 1σ error are shown in the upper part of the figure.

simulation, all the detected sources were masked from the original RASS image and the remaining pixels were bootstrapped to create a random background image, which was then Gaussian smoothed. The Moffat model was added to this image, and the fitting was repeated. We subtracted in quadrature the mean FWHM of the RASS smoothed PSF from the FWHM of each source. This quantity was defined as the source extension, with its error computed from the uncertainty on the FWHM.

4. We matched X-ray and optical sources by considering only cases where the distance between the optical and X-ray FG positions were smaller than the FWHM of the X-Ray source. Only 43 (out of 74) FG candidates have X-ray counterparts meeting this requirement.
5. We classified the FG X-ray sources as extended if the extension parameter was greater than 0 at the 2σ level (see Figure 8). This selection removes eight pointlike FG candidates, leading to a sample of 35 extended FGs. In the following section, we discuss the effect of SDSS spectroscopic incompleteness on this sample.

2.2.4. Spectroscopic Incompleteness and the Final Sample

The SDSS spectroscopy is incomplete in high-density regions due to limitations on fiber placement. We address this spectroscopic incompleteness issue as follows: for each of the 35 FG candidates, we select all galaxies with SDSS photometry fulfilling the D_{\max} criterion and with magnitudes between m and $m + 1.75$, where m is the FG r -band Petrosian magnitude. These are the galaxies that could possibly invalidate the fossilness definition. Then, we queried the SDSS DR6 and NED for spectroscopic redshifts of these possible contaminants. We found that for nine (out of 35) FG candidates, there is at least one galaxy invalidating the $\Delta(cz_{\max})$ criterion hence disqualifying the system. Using photometric redshifts, we also rejected one system with three possible contaminants having concordant redshifts within 2σ . Applying the same analysis to the eight pointlike FG candidates (see the previous section) leaves four such objects having no possible gap contaminants.

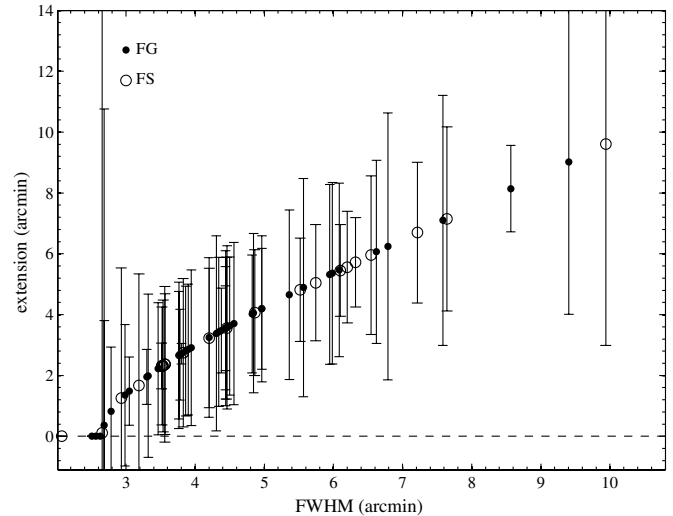


Figure 8. Extension parameter vs. FWHM for the 43 FG candidates (filled circles) with an associated X-ray source. Empty circles represent the sample of 22 field galaxies defined in Section 3. The error bars show 2σ standard uncertainties. Sources are defined as extended if their error bar does not cross the horizontal dashed line corresponding to a zero extension.

After this procedure, our final sample consists of 25 systems,¹¹ which we use to characterize the properties of FGs. This is the largest sample of FGs available in the low-redshift regime ($z < 0.1$). In Figure 9, we show the X-ray contour plots for these FGs with the optical SDSS position overlaid. As we can see, usually, the centroid of the X-ray component coincides with the optical counterpart.

2.3. Archive Data and External Comparison

We searched the *XMM*, *Chandra*, *ASCA*, and *Einstein* archives for any publicly available data, taken with any of the instruments,

¹¹ We note that almost all FGs in our sample have a total X-ray luminosity above the (bolometric) limit of $4.4 \times 10^{42} \text{ erg s}^{-1}$ adopted by Jones et al. (2003). Only two FGs (FG 11 and FG 21, see Table 2) have an X-ray luminosity of $\sim 2 \times 10^{42} \text{ erg s}^{-1}$, corresponding to a bolometric value of $\sim 3.5 \times 10^{42} \text{ erg s}^{-1}$.

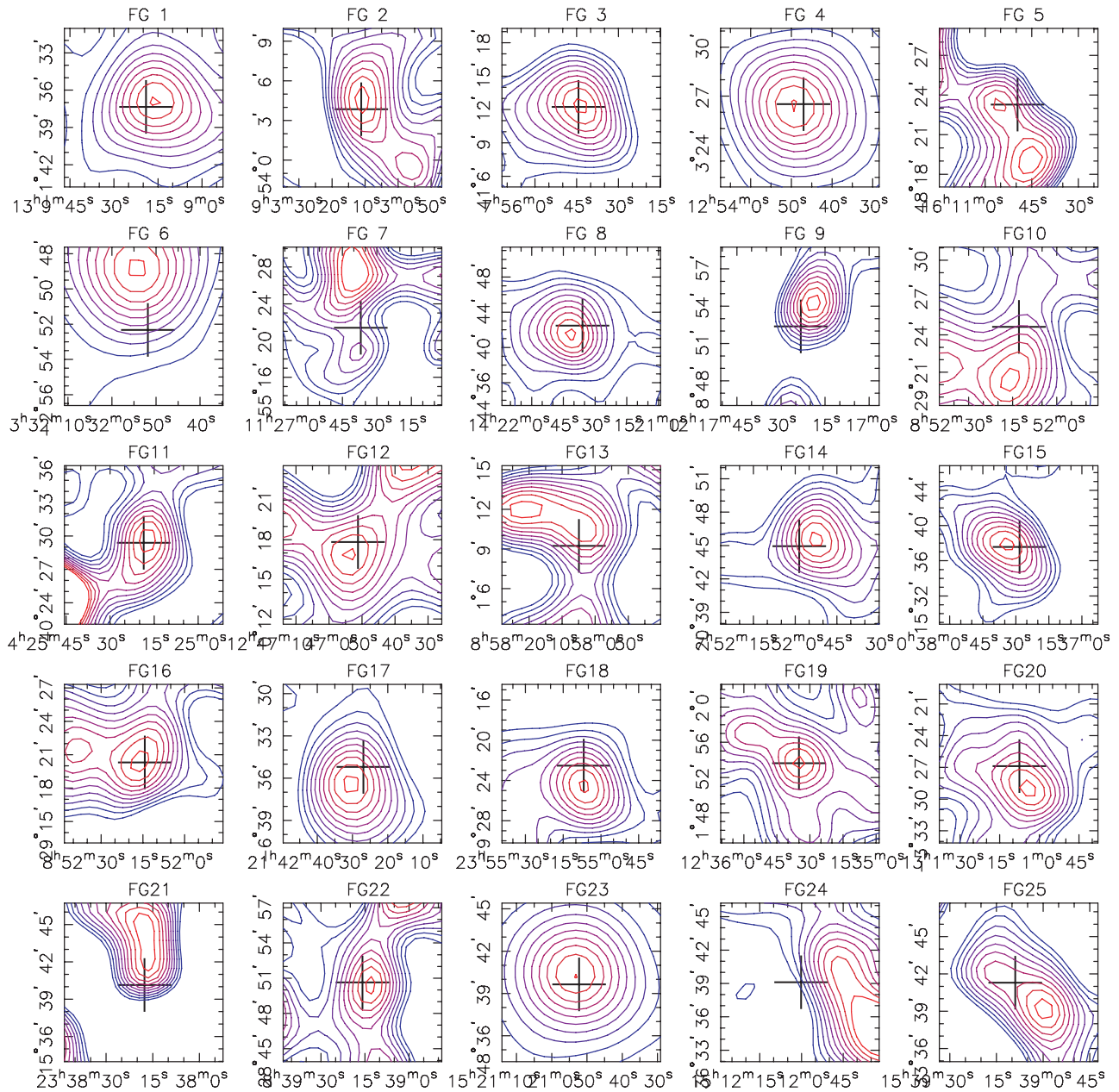


Figure 9. X-ray emission contours from the RASS for the 25 FGs, with the position of the optical SDSS galaxy image marked by a black cross. The contours have been obtained by applying a 2 pixel Gaussian smoothing to the original RASS images and are equally spaced at intervals of 1σ starting at 0.5σ above the background. The reddest contours mark the centroid of the X-ray emission. Each panel is 3 times as wide as the FWHM of the X-ray source.

(A color version of this figure is available in the online journal.)

within a $1.5 h_{75}^{-1}$ Mpc radius of the final samples of FGs and field galaxies (defined in Section 3). We found data in the vicinity of only a single FG in the *Chandra* archive. None of the other archives contained any observations including objects in our final sample. We conclude that there are no useful archival data deeper than the RASS to systematically examine the X-ray properties of our FG and field galaxies, or exclude them from the sample as X-ray AGN.

We also looked for FGs defined in the literature that are in the same redshift interval as our sample. Not surprisingly, we found only three systems well studied in several contributions (e.g., JO03; Khosroshahi et al. 2007), although none of them have data in the SDSS. Moreover, Santos et al. (2007), defining a sample of 34 FGs from SDSS-DR4, found only four systems

in the same redshift regime as we consider here. One of them is in our sample of FG candidates, but with an X-ray component indistinguishable from the RASS PSF. The other three systems are not in our FG sample because the absolute magnitude limit of our SDSS catalog prevents finding a second-rank galaxy for the main targets.

2.4. The Space Density of FGs

The space density of the 25 FGs was estimated using the $1/V_{\max}$ statistics suggested by Avni & Bahcall (1980). The sky area is that of the DR4, 4783 deg². Applying various X-ray luminosity limits we find different integrated space densities, which we compared to those of previous studies. Vikhlinin et al. (1999, hereafter V99) studying an overluminous elliptical

Table 1
Mean and Width Values of the Distributions of Several Quantities for FG and FS Galaxies^a

Quantity	FG		FS		KS
	Mean	Width	Mean	Width	
(1)	(2)	(3)	(4)	(5)	(6)
$^{0.1}M_r$	-22.64 ± 0.09	0.37 ± 0.07	-22.45 ± 0.09	0.37 ± 0.05	0.36
δ_N	2.5 ± 0.4	1.56 ± 0.30	2.5 ± 0.5	2.0 ± 0.4	0.99
$\log R_e$ (kpc)	1.13 ± 0.08	0.29 ± 0.06	0.97 ± 0.08	0.35 ± 0.10	0.23
n	5.4 ± 0.6	2.4 ± 0.6	5.5 ± 0.6	2.5 ± 0.4	0.83
$a_4 * 100$	0.11 ± 0.26	0.6 ± 0.3	0.3 ± 0.2	0.75 ± 0.11	1.00
$\nabla(g-r)$	-0.072 ± 0.026	0.09 ± 0.06	-0.17 ± 0.08	0.25 ± 0.08	0.74
$\log L_X (\cdot 10^{44} h_{75}^{-2} \text{ erg s}^{-1})$	-0.90 ± 0.09	0.41 ± 0.13	-0.84 ± 0.15	0.52 ± 0.11	0.44
δ_{CM}	0.0 ± 0.3	0.8 ± 0.4	-0.5 ± 0.3	1.1 ± 0.2	0.29
$\log \sigma_0$ (km s ⁻¹)	2.43 ± 0.01	0.07 ± 0.01	2.42 ± 0.04	0.09 ± 0.05	0.40
$\log \text{Age}$ (Gyr)	0.72 ± 0.03	0.14 ± 0.03	0.77 ± 0.04	0.16 ± 0.04	0.10
$[Z/H]$	0.44 ± 0.03	0.17 ± 0.02	0.34 ± 0.06	0.24 ± 0.05	0.29
$[\alpha/Fe]$	0.27 ± 0.02	0.10 ± 0.01	0.28 ± 0.03	0.12 ± 0.02	0.93

Note. ^a The p values from the KS test comparing the distributions of FG and FS properties are reported in Column 6. Values smaller than 0.1 indicate that the two samples likely do not derive from the same parent distribution.

galaxy (OLEG) sample found a space density of $1.5 \times 10^{-6} h_{75}^3 \text{ Mpc}^{-3}$ for $L_X > 0.44 \times 10^{42} h_{75}^{-2} \text{ erg s}^{-1}$ while we find $3.4 \times 10^{-6} h_{75}^3 \text{ Mpc}^{-3}$. For the same limiting value of L_X , Romer et al. (2000) found $6.7 \times 10^{-6} h_{75}^3 \text{ Mpc}^{-3}$, JO03 found $6.75 \times 10^{-7} h_{75}^3 \text{ Mpc}^{-3}$, and Dariush et al. (2007) predicted $5.4 \times 10^{-6} h_{75}^3 \text{ Mpc}^{-3}$ based on the Millennium simulation. Considering the errors in these measurements, as presented in Table 1 of JO03, we can conclude that all these values are consistent. When a brighter limiting L_X is considered, $L_X > 0.89 \times 10^{42} h_{75}^{-2} \text{ erg s}^{-1}$, V99 found $8.1 \times 10^{-6} h_{75}^3 \text{ Mpc}^{-3}$ and we find $2.83 \times 10^{-6} h_{75}^3 \text{ Mpc}^{-3}$, still consistent. We emphasize that the samples analyzed by R00, V99, and JO03 have only 3, 4, and 5 systems, respectively, while we have 25 new FGs, yet the space densities are still very consistent.

3. COMPARING THE PROPERTIES OF FGS AND FIELD GALAXIES

To establish a benchmark for the properties of FGs, we generated a control sample of galaxies with the same luminosity distribution and the same optical and X-ray properties as the FG sample. The control sample represents an idealization of a sample of systems which were probably formed by a single collapse of a protogalaxy and did not experience any major mergers in last 3–4 Gyr. From now on, we refer to the control sample as “field” galaxies. This was created by first excluding the brightest galaxies of the FG optical candidates and their companions (see Section 2.1) from the whole galaxy catalog, yielding a reduced catalog with 90,259 targets. We binned the sample of 578 FG optical candidates and the reduced galaxy catalog by r -band absolute magnitude, and for each bin computed the ratio between the number N_1 of FG optical candidates in that bin to the number N_2 of galaxies in the reduced catalog. Galaxy absolute magnitudes were computed as described in Appendix B. To obtain a sample of “field” galaxies with the same LF as that of the seed galaxies of the 578 optical FG candidates, we randomly extracted galaxies from the reduced catalog in each magnitude bin according to the corresponding value of the ratio $f = N_1/N_2$. Because we have excluded the brightest galaxies and their companion galaxies in the optical FG candidates from the entire galaxy catalog, it is possible for N_2 to be lower than N_1 , yielding an ill-defined

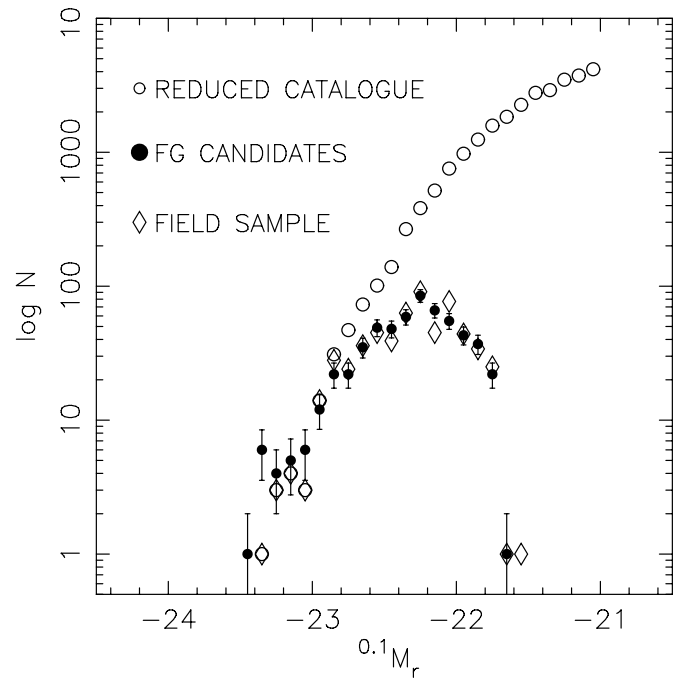


Figure 10. LFs of galaxies in the reduced catalog (empty circles), brightest galaxies in FG candidates (filled circles) and of galaxies in the field sample (diamonds). The symbols used for each sample are shown in the upper left part of the figure. The error bars mark 1σ Poissonian uncertainties on number counts of FG brightest galaxies.

value of f . This is shown in Figure 10, where we compare the LF of the brightest galaxies in the optical FG candidates with that of galaxies in the reduced catalog. At magnitudes brighter than $M_r \sim -23$, the number of optical FG candidates in each magnitude bin is slightly larger than the number of galaxies in the reduced catalog. To ensure that the value of f is always less than one, we enlarged the size of the brightest magnitude bins such that the condition $N_2 < N_1$ was always fulfilled. This goal was achieved by considering the same magnitude bins as in Figure 10 for $M_r \gtrsim -22.8$, and just one bin at brighter magnitudes, from $M_r = -23.6$ to $M_r \sim -22.8$. The list of field galaxies was extracted according to this binning procedure, and, by construction, it has the same sample size ($N = 578$) as the

optical FG candidates. Figure 10, which also plots the LF of this field sample, shows that its LF actually matches the LF of the seed galaxies in the optical FG candidates. As expected from the fact that we use a single, larger magnitude bin at $M_r \lesssim -23$, there is only a small difference between the two LFs in this magnitude range. However, this difference is only marginally significant, provided that uncertainties on number counts are taken into account.

To perform a detailed comparison between FGs and field galaxies, we extracted a subsample of field galaxies, following the same procedure adopted to select the sample of FGs from the initial list of 578 optical FG candidates (see Section 2.2). We removed spirals and AGNs from the catalog of field galaxies, and analyzed the X-ray images of the remaining systems. Sixty-six (out of 578) field galaxies have significant X-ray detections. From these, following the prescriptions outlined in the previous section, we kept only the 22 galaxies associated with an X-ray source and with a projected distance from rich Abell clusters larger than 1.5 Mpc. Applying the X-ray extent requirement leaves a final sample of 17 field galaxies, shown in Figure 8. A similar analysis to that performed in Section 2.2.2 for FGs shows that contamination from elusive AGN and starbursts is also negligible for the sample of field galaxies (see Figure 6). Although selected in the same way from an optical catalog with the same number of galaxies (578) and the same galaxy LF as the FGs, the number of galaxies in the field sample with significant X-ray detections ($N = 66$) is 65% less than the corresponding FG sample ($N = 102$). The final FG and field samples have a similar ratio of 68%.

In the following sections, we compare the distributions of several properties (luminosity, structural parameters, internal color gradients, stellar populations) of FG and field galaxies. For each quantity, the comparison is performed (1) by a Kolmogorov–Smirnov (hereafter KS) test and (2) by deriving the mean and width of each distribution. The mean and width values obtained for each quantity and the results of the KS tests are reported in Table 1. In order to reduce the effects of outliers in each distribution, the corresponding mean, and width values were computed using a 2.5σ clipping method. We also verified that computing the location and width values with statistical software ROSTAT (Beers et al. 1990) does not affect our results. All quantities used in this analysis are reported in Table 2 for each FG and field galaxy (see Appendix A). Although not used in the present analysis, the table also lists the properties of the four FGs with pointlike X-ray emission that survived the final section step described in Section 2.2.4. The distributions of photometric and X-ray properties of FGs and field galaxies (hereafter also referred to as the field sample, FS) are presented in Figure 11 and described in the following sections.

4. LUMINOSITIES OF FIRST- AND SECOND-RANK GALAXIES

In this section, we analyze the properties of FGs by examining the magnitude distributions of their seed and second-rank galaxies as well as their X-ray fluxes.

Figure 11(a) compares the optical luminosity distributions of FGs first-rank galaxies with those of the corresponding field sample. The mean and width values of each distribution are reported in Table 1. Both the figure and the table show that the r -band LFs of FG and field galaxies are indistinguishable. This result is also confirmed by the KS test (see Table 1), whose p value is $\gtrsim 0.3$. Figure 11(b) shows that not only the optical but also the X-ray luminosities of FG galaxies are consistent with

those of field galaxies. This is also clear from the mean, width, and KS test results reported in Table 1. The fact that FG and field galaxies have the same X-ray luminosities is of particular interest, since it implies that both samples consist of galaxies embedded within halos of the same mass. Hence, any difference between FG and field samples is not related to the selection of these samples, but is more deeply related either to the initial conditions of the galaxy LF within the halos, or to the different evolutionary histories of galaxies within the halo.

To analyze the luminosity distribution of second-rank galaxies, we have to consider that the SDSS-DR4 galaxy catalog is magnitude limited and that FG optical candidates are selected as systems where the magnitude difference between the two brightest galaxies is greater than ΔM_{\min} . This implies that a larger fraction of FGs can be selected at the brightest magnitudes of the galaxy LF. In other words, the seed galaxies of FGs do not form a magnitude complete sample. Such incompleteness is illustrated in Figure 12, where we plot the magnitude difference ΔM between the second and first-rank galaxies of FGs as a function of the r -band absolute magnitude, $^{0.1}M_r$, of the first-rank galaxy. Absolute magnitudes are obtained as described in Appendix B, by k -correcting the Petrosian r -band magnitudes of the DR4 data set to redshift $z = 0.1$. Since the SDSS galaxy catalog is limited to $M_r = -20$, and since, by definition, we have $\Delta M > \Delta M_{\min} = 1.75$ mag, the seed galaxies of FGs have to fulfill the equation

$$^{0.1}M_r + ^{0.1}k_r < -20 - \Delta M \sim -21.75 \text{ mag.} \quad (1)$$

The term $^{0.1}k_r$ denotes the k -correction computed as described in Appendix B, and is introduced in the previous equation to account for the fact that k -corrections were not applied in the computation of the r -band absolute magnitudes used to select the SDSS-DR4 catalog. Since the typical value of k_r is -0.13 mag, Equation (1) implies the constraint $^{0.1}M_r \lesssim -21.62$, and in fact, as shown in Figure 12, we do not find any first-rank galaxy fainter than this magnitude limit. Moreover, for a given value of $^{0.1}M_r$, we can only select FGs with $^{0.1}M_r + ^{0.1}k_r + \Delta M < -20$, which implies $\Delta M < -^{0.1}M_r - 20 - ^{0.1}k_r \sim -^{0.1}M_r - 19.87$. This last constraint is shown by the line in Figure 12, and results in a larger range of allowed values of ΔM at bright galaxy magnitudes. In other words, the selection procedure affects the magnitude distribution of FGs, biasing the sample toward a larger allowed fraction of systems at brighter magnitudes. Despite this bias, Figure 12 shows that the brightest first-rank galaxies do not show a larger range of ΔM values, although they are allowed. At bright magnitudes, we see that seed galaxies of FGs are characterized by a larger magnitude gap. However, one has to note that the SDSS spectroscopic incompleteness due to fiber collisions might cause an overestimate of ΔM , and that the SDSS spectroscopic survey did not target many very bright galaxies ($r < 15.5$), which might reduce the number of detected FG systems at the bright end.

To better understand the distribution of ΔM with respect to the magnitude of the seed galaxies, we ran Monte Carlo simulations. For each seed galaxy of the 102 FG candidates, we assigned a fictitious second-rank galaxy from the SDSS catalog by randomly extracting a galaxy with $\Delta M \geq \Delta M_{\min}$. We repeated this procedure several times ($N = 10,000$), and estimated the mean value of ΔM obtained for the randomized second-rank galaxies. Figure 12 shows that this mean ΔM value actually decreases as $^{0.1}M_r$ increases. At magnitudes fainter than $^{0.1}M_r \sim -23$, the simulated ΔM value is fully consistent with the ΔM distribution of FGs, implying that the ΔM versus

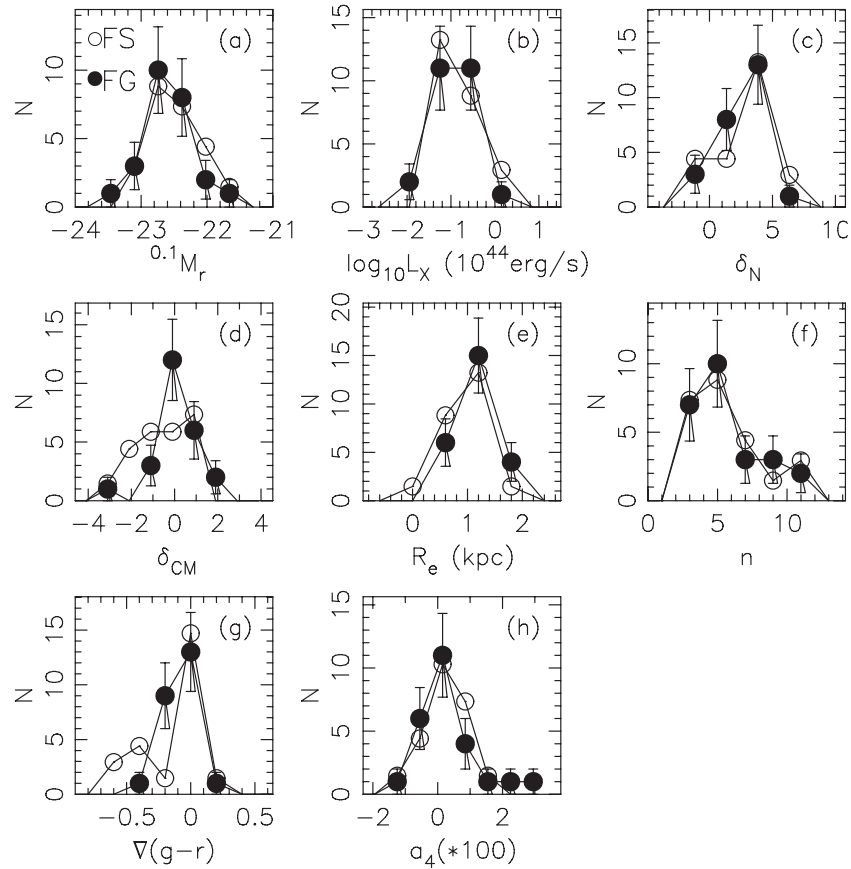


Figure 11. Distributions of FG and FS properties as follows: (a) absolute magnitude, (b) X-ray luminosity, (c) density excess, (d) normalized distance to the red sequence, (e) r -band effective radius, (f) r -band Sersic index, (g) internal color gradient, and (h) boxiness parameter. FG and field galaxies are plotted as filled and empty circles, respectively (see the upper left panel). Error bars mark the 1σ standard confidence intervals of FG number counts. To make the plot more readable, uncertainties on field galaxy number counts are not shown. The distribution of field galaxies is normalized to the total number of corresponding FG galaxies.

$^{0.1}M_r$ correlation can be simply explained by the shape of the LF of second-rank galaxies. However, at bright magnitudes ($^{0.1}M_r < -23$), all the seed galaxies of FGs have ΔM values larger than the simulations, which might reflect some intrinsic physical property of FG systems (see Section 9).

5. FAINTEST GALAXIES: DENSITY EXCESS

We characterize the population of the faintest galaxies around each FG by measuring the density excess of these galaxies with respect to the field population. Since galaxies around FGs can be fainter than the magnitude limit of the SDSS spectroscopic catalog, we measure the density excess by taking advantage of the SDSS-DR4 photometric data, whose completeness limit¹² is ~ 22.2 mag in the r -band (Stoughton et al. 2002). The density excess, δ_N , is defined as follows:

$$\delta_N = \frac{\rho_{\text{in}} - \rho_{\text{out}}}{\sqrt{\sigma_{\text{in}}^2 + \sigma_{\text{out}}^2}}, \quad (2)$$

where ρ_{in} is the mean galaxy density within a inner circle of radius r_{in} centered on the FG seed galaxy and ρ_{out} is the mean galaxy density in a concentric annulus with inner and outer radii of r_1 and r_2 , respectively. The quantities σ_{in} and σ_{out} denote the 1σ uncertainties on ρ_{in} and ρ_{out} , which are estimated by accounting for Poisson noise in the galaxy counts. For each

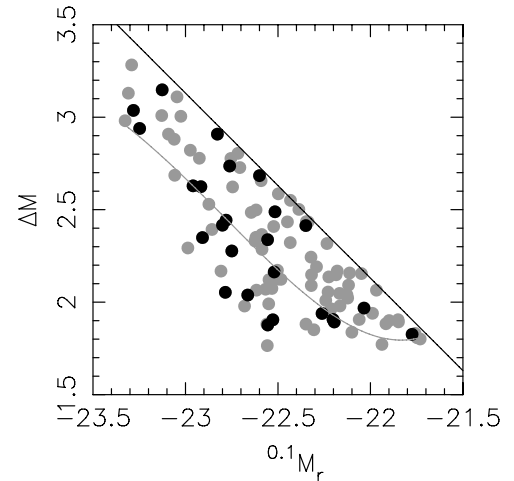


Figure 12. Differences between r -band magnitudes of second- and first-rank galaxies of FGs, ΔM , are plotted as a function of the absolute magnitude, $^{0.1}M_r$, of the first-rank galaxies. Gray circles denote the sample of 102 FG candidates with X-ray significant detection (see Section 2.2), while black symbols correspond to the final sample of 25 FGs. The black line marks the range of allowed values of ΔM as a function of $^{0.1}M_r$, while the gray curve shows the mean ΔM value as a function of $^{0.1}M_r$, obtained by randomly extracting second-rank galaxies from the SDSS catalog (see the text).

FG, we measure δ_N by setting $r_{\text{in}} = 0.25R_{\text{Abell}}$, $r_1 = 1R_{\text{Abell}}$ and $r_2 = 2R_{\text{Abell}}$, respectively, where R_{Abell} is the apparent size corresponding to one Abell radius (1.5 Mpc) at the redshift

¹² This is defined as 95% detectability for pointlike sources.

of the FG seed galaxy. We have verified that our results do not change when these radii are varied by as much as 20%. To probe a fixed range of the galaxy LF, we measure ρ_{in} and ρ_{out} using only galaxies in the magnitude range of m_2 to $m_2 + 2$, where m_2 is the magnitude of the second-rank galaxy in each FG.

Figure 11(c) compares the δ_N distributions of FGs and field galaxies. Since we do not have second-rank galaxies for the field sample, we obtained the corresponding density excesses as follows. For each field galaxy with apparent and absolute magnitudes m_r and $^{0.1}M_r$, we randomly assign a magnitude shift ΔM following the distribution of magnitude differences between first and second-rank galaxies of the 102 FG candidates (see Figure 12). Then, we set $m_2 = m_r + \Delta M$, and measure the density excess around the field galaxy following the procedure outlined above. In other words, we assign a fictitious second-rank galaxy to each field galaxy according to the magnitude distribution of first and second-rank galaxies in the sample of 102 FG candidates. Figure 11(c) shows that most galaxies in each sample tend to have positive δ_N values. In fact, as shown in Table 1, the mean value of the density excess is about 2.5 for both samples, and, considering the corresponding uncertainty, is always significantly larger than zero. This implies that there is an excess of faint galaxies in the surrounding regions of both FG and field galaxies. Both Figure 11(c) and the mean and width values reported in Table 1 show that the distributions of δ_N values of FG and field galaxies are fully consistent.

6. FGs AND THE RED SEQUENCE

The distribution of FG seed galaxies in color–magnitude space can provide clues to their formation history. We characterize the $g - r$ versus r color–magnitude relation of early-type galaxies as described in Appendix B, and then compare the distribution of FG and field galaxies to that relation. It is implicit in this simple analysis that the red sequence mainly originates from a mass–metallicity relation (see e.g., Kodama et al. 1998), and that galaxies lying on the sequence represent, as a first approximation, passively evolving systems that have not experienced recent episodes of star formation. By measuring how distant the colors of FGs are from the color–magnitude relation, we have an indication of how star formation is evolving in these systems.

We compute the distance δ_{CM} of the colors of FG and field galaxies to the red sequence as

$$\delta_{\text{CM}} = \frac{[(g - r) - (a + b \times ^{0.1}M_r)]}{\sigma_{g-r}(^{0.1}M_r)}, \quad (3)$$

where a and b are the offset and slope of the color–magnitude relation, and $\sigma_{g-r}(^{0.1}M_r)$ is the scatter about the red sequence (see Equation (B1) of Appendix B). Figure 11(d) compares the δ_{CM} distribution of FG and field samples, with the corresponding mean and width values tabulated in Table 1. The results of the KS test, comparing the δ_{CM} distributions, is also reported in the same table. We see that the δ_{CM} distributions are always peaked near zero, as one would expect since FGs and field galaxies are morphologically selected as early-type systems. Figure 11(d) suggests that field galaxies have a broader distribution than FGs. However, the corresponding mean values are fully consistent with zero and their widths are consistent with unity, implying no significant difference between the δ_{CM} distributions. This result is also confirmed by the p value from the KS test.

7. STRUCTURAL PROPERTIES AND COLOR GRADIENTS

We analyze the surface brightness distribution of FG seed galaxies by studying (1) their structural parameters and internal color gradients and (2) the departures of galaxy isophotes from purely elliptical shapes. Internal color gradients are estimated using the structural parameters of galaxies, specifically the effective radius, r_e , and the Sersic index (shape parameter), n , while galaxy isophotes are characterized using the a_4 parameter that describes boxy/disky departures of the isophotes from elliptical shapes (Bender & Möllenhoff 1987). The derivation of these quantities is described in C.

Figures 11(e) and (f) compare the distributions of effective radii and shape parameters for FG and field galaxies. The mean and width values of FGs and the field sample (see Table 1) are fully consistent, with the p values of the KS tests greater than ~ 0.2 . The lack of galaxies with Sersic index $n \gtrsim 2$ is a natural consequence of our sample consisting of morphologically selected early-type galaxies. Although the Sersic index does not provide a precise measurement of the bulge to disk ratio of a galaxy, it can effectively separate disk and bulge dominated systems, with $n \sim 2$ as the dividing value between the two classes (e.g., Blanton et al. 2005).

Figure 11(g) compares the distributions of color gradients, $\nabla(g - r)$, for FG and field galaxies. We find that fossils and field galaxies have a consistent mean color gradient of $\nabla(g - r) \sim -0.07$, but the scatter of field galaxies around the mean value is somewhat larger than that of FGs (see Table 1). The difference between the width values of the two samples is 0.16 ± 0.1 , which is (marginally) greater than zero by 1.6σ . The KS test (Table 1) confirms that there is no significant difference between the two samples. Our color gradient estimates can be directly compared with those of La Barbera et al. (2005), who derived the mean $g - r$ color gradient in early-type galaxies in clusters of different richnesses at different redshifts. For galaxies in poor groups at a redshift of $z \sim 0.08$, close to the median redshift of our FG and FS samples, they found a mean color gradient of $-0.064_{-0.02}^{+0.008}$ (see their Table 1), agreeing with the mean $\nabla(g - r)$ values reported in Table 1. The mean value of $\nabla(g - r)$ has also been measured from SDSS data by Wu et al. (2005), who analyzed a sample of 36 early-type galaxies at $z \sim 0.02$. They find a mean $\nabla(g - r)$ value of -0.05 ± 0.01 (see their Table 3), which differs by less than 2σ from the results in Table 1.

In Figure 11(h), we compare the distributions of a_4 values for FG and field galaxies. Looking at the mean and width values reported in Table 1, as well as at the KS test results reported in Table 1, the distributions for FG and field galaxies are again fully consistent. The distribution of a_4 values carries interesting clues about the formation of FG galaxies. Analyzing the isophotal shapes of seven FG galaxies drawn from the sample of Jones et al. (2003), Khosroshahi et al. (2006, hereafter KPJ06) found that all FG galaxies tend to have disk isophotes. In more detail, examining Figure 3, three (of seven) FGs in the KPJ06 sample have a_4 values very close to zero, with the remaining four galaxies having significantly larger values. In our sample, we find that the distribution of FGs is peaked around $a_4 = 0$, with equal numbers of disk and boxy systems. The disagreement we find with KPJ06 may reflect the small sample analyzed in that study. Our comparison of FG and field galaxies shows no difference in isophotal deviations from elliptical shapes. In other words, FG galaxies do not have peculiar isophotes when compared to “normal” field galaxies.

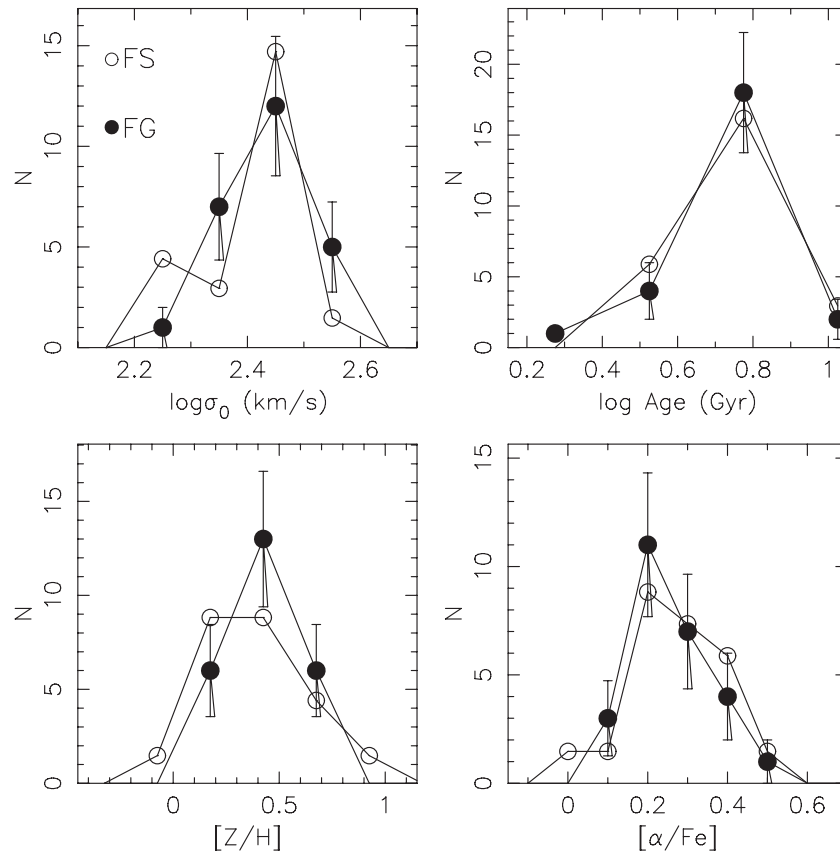


Figure 13. Same as Figure 11 but comparing velocity dispersions and stellar population parameters for FG and field galaxies.

8. STELLAR POPULATIONS

To analyze the stellar populations of FGs and field galaxies, we use spectra from the SDSS-DR4 with a resolution of 4.42 \AA (FWHM). For each galaxy, we search for the single stellar population (SSP) model that best matches the galaxy spectrum. The matching is performed using measurements of spectral indices, resulting in estimates of age, metallicity, and elemental abundance ratios $[\alpha/\text{Fe}]$. The procedure consists of (1) estimating the spectral indices and (2) extracting the stellar population parameters, as detailed in Appendix D.

Velocity dispersions and stellar population parameters for FGs and field galaxies are reported in Table 2. The distributions of σ , age, $[\text{Z}/\text{H}]$, and $[\alpha/\text{Fe}]$ are shown in Figure 13, with the corresponding mean and width values, and the KS test being reported in Table 1. We see that the distributions of FGs and field samples are fully consistent, with the p value of the KS test being larger than ~ 0.1 . Figure 14 shows how stellar population parameters vary as a function of velocity dispersion for both FGs and field galaxies. We see that both samples follow the same correlation between $[\alpha/\text{Fe}]$ and velocity dispersion, as found from previous studies for field galaxies (e.g., de la Rosa et al. 2007). Moreover, both FGs and field galaxies occupy the same region in the diagrams of age and metallicity versus velocity dispersion, emphasizing the similarity of both samples. In Figure 14, we also insert the stellar population parameters for the twenty elliptical galaxies in Hickson compact groups (HCGs) analyzed by de la Rosa et al. (2007). The stellar population parameters of these galaxies were remeasured following the same procedure as for FGs and field galaxies. Note that ellipticals in HCGs

have higher ages and lower metallicities than both FGs and field galaxies, showing no correlation between $[\alpha/\text{Fe}]$ and velocity dispersion.

9. DISCUSSION

In the current hierarchical model of galaxy formation, the basic idea is that massive galaxies form later as a result of the merging history of their dark matter halos, but their stars form earlier (downsizing). In this sense special attention is being focused on massive (luminous) galactic systems, whether they reside in low- or high-density locations. We may find fossils at different cosmic epochs, and they provide important clues that help us distinguish between nature and nurture. Our main results from this paper are as follows.

We found 578 candidates following our optical photometric definition of FGs in the redshift range $0.05 < z < 0.095$. After discarding incorrect morphological classifications and AGNs we are left with 102 FGs for which there is a significant X-ray detection in *ROSAT* (maximum total flux of $10^{-14} \text{ erg cm}^{-2} \text{ s}^{-1}$). Only 25 FGs were selected with likely extended X-ray emission and not associated with rich clusters. These constitute our final sample of FGs. Applying the V/V_{max} test we find a spatial density of $2.83 \times 10^{-6} h_{75}^3 \text{ Mpc}^{-3}$, comparable to three other independent observational studies (V99, RO00, and JO03) and to the recent analysis of the Millennium Simulation by Dariush et al. (2007).

As shown in Figure 12, the brighter FGs always have ΔM greater than ~ 3.0 mag while fainter FGs are limited by the completeness of the SDSS catalog. The lack of systems in the lower left part of the figure, at magnitudes brighter than

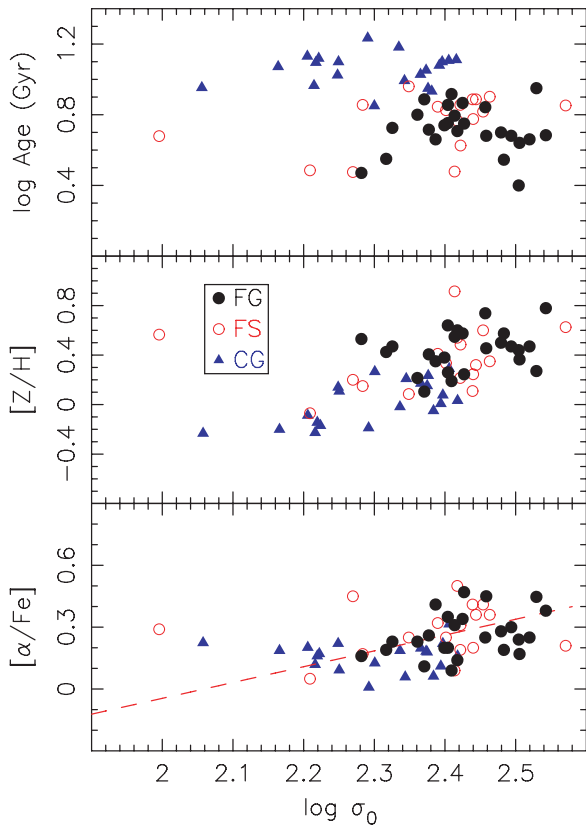


Figure 14. Correlations of stellar population parameters with velocity dispersion for FGs, field galaxies, and galaxies in Hickson Compact Groups, represented with different symbols as shown from the inset in the middle panel. In the bottom figure, as an aid to the discussion, the best fit to the sample of 66 field galaxies (see Section 3) is plotted (dashed line). Values of stellar population parameters from the de la Rosa et al. (2007) have been transformed to the α -models system used here (see Appendix D).

(A color version of this figure is available in the online journal.)

$^{0.1}M_r \sim -23$, might be caused by selection effects as well as by the shape of the galaxy LF. Thus, it is not clear from the present analysis if the absence of systems in the lower left part of Figure 12 is related to some physical characteristics of the sample. It would be reasonable to expect that as mergers progress the LF of such systems will have a larger gap between the first and the second-ranked galaxies.

The density excess around FGs is fully consistent with what we measure for field galaxies, implying that the environments around both systems are statistically identical when considering the faint galaxy population. This result seems to indicate that FGs and field galaxies originate from similarly overdense regions of the large-scale structure.

By studying the distribution of color offsets from the red sequence, we find that FGs occupy a similar region to field ellipticals. We also find that the mean color gradients in both samples (FG and FS) are statistically the same. However, the scatter around the mean for FGs is significantly (1.6σ) smaller than that for field ellipticals, which may indicate a more regular process in the buildup of FGs, such as mergers of L^* galaxies. The distribution of a_4 , which measures isophotal shape deviations from a pure ellipse, indicates that FGs and field ellipticals are similar.

Studying the stellar populations in the 25 FGs and 17 field galaxies we find that there is no difference in age, metallicity, or α -enhancement, indicating that the star formation history of

fossil groups seems to be analogous to that of field ellipticals. We further examined elliptical galaxies in compact groups studied by de la Rosa et al. (2007). As already established in previous works, elliptical galaxies in CGs are older and more metal poor than field ellipticals (Proctor et al. 2004; de la Rosa et al. 2007) and fossil groups. Particularly, when we look at the relation between $[Z/H]$ and $\log \sigma$, the mass–metallicity relation is evident (see Lee et al. 2006; Kobayashi 2005). More massive galaxies (in both FGs and field galaxies) retain their metals more efficiently than the low mass ones (i.e., ellipticals in CGs). The α -enhancement diagram shows a clear trend between α/F_e and velocity dispersion (mass). This can be interpreted as a manifestation of downsizing—the less massive galaxies have a more extended star formation history. Based on these results we see that FGs are similar to field ellipticals but cannot be formed by dry mergers of ellipticals in a CG. However, a wet merger with a gas-rich disk system may also explain the observed relations. Here, the luminosity weighted parameters (Age, $[Z/H]$, $[\alpha/Fe]$) are more sensitive to the recent star formed population, generating lower ages, higher $[Z/H]$ and higher $[Mg/Fe]$. This assumes that the merger starburst is soon followed by SN/AGN feedback, which depletes the gas content.

McCarthy et al. (2004) have found a significant population of red galaxies at high redshift ($1.3 < z < 2.2$), and claim that they cannot be descendants of the $z \sim 3$ Lyman-break galaxies. Based on their spectroscopic data they also conclude that most of the present-day massive galaxies had an early ($z_f = 2.4$) and rapid formation. If we restrict ourselves to the 25 FGs, their last main star formation episode must have occurred at $z > 0.3$, much more recently than in the high- z galaxies. It appears that a more recent burst occurred in the FGs which would explain their lower ages. Therefore, we may be seeing massive ellipticals that accreted a small galaxy at $z > 0.3$.

Our results indicate that FGs are not significantly different from bright ellipticals found in low-density regions of the universe. As claimed by Mulchaey & Zabludoff (1999) in a detailed study of NGC 1132, FGs could simply be “failed” groups—a few relatively bright galaxies merged forming the dominant system we see today, but without enough surrounding matter to form additional nearby bright galaxies, resulting in an atypical LF. This is also in agreement with recent results obtained by D’Onghia et al. (2005) based on N -body/hydrodynamical cosmological simulations where they find that FGs are formed by the infall of $L \sim L_*$ systems along filaments with impact parameters as small as 5 kpc.

Our findings suggest that the objects meeting the observational criteria expected for fossil groups at low redshift might not be true fossils. The extensive study presented here whereby we select FG candidates based on optical data, and then examining their X-ray counterparts reveals no difference between FGs and field ellipticals. We note that fossils can be created anytime in cosmic history, and these systems may represent the final stage of mass assembly as suggested in the analysis of the Millennium simulation by Dariush et al. (2007), instead of forming a distinct class.

We thank the referee for several comments that helped to significantly improve this paper. We acknowledge Dr. D. Kocevski for helping us with X-ray analysis of the RASS data. G.S. and A.R. thank the EC and the MIUR for having partially supported this work (EC contracts HPRN-CT-2002-00316–SISCO network, and MIUR-COFIN-2004 n.2004020323_001).

Table 2
Properties of FG and FS Galaxies

ID	R.A.	Dec.	z	$^{0.1}M_r$	ΔM	$^{0.1}g-r$	δ_N	$r_{e,g}$	$r_{e,r}$	n_g	n_r	$a_4(\times 100)$	$\nabla(g-r)$	$\log L_X$	δ_{CM}	$\log \sigma_0$	$\log Age$	$[Z/H]$	$[\alpha/Fe]$	FLAG
(1)	(2)	(3)	(4)	(5)	(6)	(7)	(8)	(9)	(10)	(11)	(12)	(13)	(14)	(15)	(16)	(17)	(18)	(19)	(20)	(21)
1	197.32954	-1.6225	0.083	-22.917	2.62	1.020	2.6	9.11	8.09	4.1	3.0	0.24	-0.068	0.09	1.894	2.494	0.7	0.47	0.30	1
2	135.79644	54.0643	0.083	-22.663	2.04	0.988	3.0	4.14	5.36	4.0	3.8	-0.20	-0.061	-1.00	0.360	2.479	0.7	0.50	0.28	1
3	118.93488	41.2039	0.074	-22.908	2.35	0.965	3.3	5.66	5.82	5.4	4.5	-0.26	-0.024	-1.05	-0.935	2.404	0.9	0.26	0.20	1
4	193.44587	3.4418	0.066	-22.349	2.41	0.802	-0.8	4.52	4.18	5.4	4.3	0.14	0.042	-0.60	-4.846	2.504	0.4	0.44	0.24	1
5	242.70645	48.3879	0.090	-22.203	1.91	0.956	-0.8	45.14	102.19	8.0	9.8	-0.30	0.093	-0.27	-0.338	2.317	0.6	0.42	0.19	1
6	202.96613	-2.8721	0.086	-22.556	2.34	0.961	3.9	4.49	6.11	5.8	5.5	0.99	-0.041	-0.76	-0.490	2.377	0.7	0.41	0.26	1
7	171.65402	55.3564	0.070	-22.528	1.90	0.960	1.5	300.11	22.26	6.3	4.2	-0.28	-1.155	-0.90	-0.509	2.414	0.8	0.55	0.31	1
8	215.39972	44.7081	0.091	-22.781	2.44	1.006	2.8	26.16	49.60	8.6	8.6	0.97	0.089	-0.80	1.041	2.483	0.5	0.57	0.19	1
9	184.34689	8.8729	0.094	-22.785	2.05	0.952	3.0	37.91	27.49	3.9	3.2	-0.49	-0.487	-0.53	-1.194	2.427	0.7	0.24	0.47	1
10	133.05354	29.4108	0.086	-22.959	2.63	0.970	2.3	13.98	35.33	2.3	3.4	1.29	0.297	-0.76	-0.781	2.399	0.7	0.38	0.20	1
11	216.32744	40.4898	0.083	-22.035	1.97	0.964	-0.0	10.82	12.82	4.8	4.5	0.48	-0.115	-1.70	-0.038	2.326	0.7	0.47	0.23	1
12	191.71340	0.2970	0.089	-23.248	2.94	1.006	4.0	20.44	14.73	7.5	6.0	-0.56	-0.271	-0.65	1.150	2.505	0.6	0.36	0.17	1
13	134.52059	1.1537	0.071	-22.262	1.94	0.997	2.2	26.81	25.39	9.4	9.0	-0.03	-0.108	-1.19	0.727	2.404	0.8	0.64	0.35	1
14	117.99395	20.7490	0.077	-21.775	1.83	0.954	1.3	7.37	8.38	4.5	4.2	1.14	-0.102	-1.04	-0.145	2.282	0.5	0.53	0.16	1
15	9.36782	15.6263	0.080	-22.800	2.42	0.987	2.0	11.72	10.64	6.4	5.1	-0.06	-0.096	-1.15	0.260	2.371	0.9	0.10	0.11	1
16	133.05970	29.3385	0.085	-22.196	1.89	0.993	2.3	8.64	12.85	6.1	6.5	0.15	-0.046	-1.04	0.646	2.457	0.8	0.74	0.25	1
17	325.61206	-6.5868	0.088	-22.750	2.28	0.979	3.4	26.36	35.56	9.9	10.2	2.42	-0.070	-0.93	-0.050	2.409	0.9	0.19	0.09	1
18	358.77843	-9.3756	0.074	-22.516	2.49	0.981	4.2	4.28	4.92	3.6	3.6	0.66	-0.139	-0.98	0.168	2.387	0.7	0.35	0.41	1
19	188.89591	1.8937	0.078	-22.520	2.16	1.025	3.6	37.61	25.27	8.6	7.0	-0.01	-0.223	-1.04	1.568	2.520	0.7	0.47	0.25	1
20	195.28142	-3.4480	0.083	-22.761	2.74	1.007	5.6	10.16	12.72	4.9	4.7	0.46	-0.086	-1.11	1.070	2.425	0.9	0.57	0.34	1
21	354.57353	15.6689	0.066	-22.600	2.68	0.973	1.7	8.45	14.56	2.7	4.0	2.66	0.044	-1.77	-0.122	2.361	0.8	0.21	0.23	1
22	129.81595	28.8441	0.079	-23.281	3.04	0.993	4.6	4.51	6.14	2.1	2.4	0.20	-0.203	-1.10	0.122	2.543	0.7	0.78	0.38	1
23	230.21770	48.6607	0.074	-23.126	3.15	0.943	4.0	10.66	12.67	4.7	4.8	-0.72	-0.102	-0.40	-3.176	2.529	1.0	0.27	0.45	1
24	228.00073	36.6520	0.066	-22.827	2.91	0.980	0.9	11.04	14.23	3.2	3.3	-1.16	0.059	-0.49	-0.078	2.417	0.7	0.60	0.14	1
25	234.78742	33.6881	0.070	-22.555	1.88	1.016	3.8	20.37	20.19	9.9	10.4	0.09	-0.129	-0.84	1.299	2.458	0.7	0.46	0.45	1
26	172.88388	12.6997	0.081	-22.306	1.85	0.972	1.0	7.00	9.99	2.4	2.6	-0.04	-0.108	-1.23	0.017	2.434	0.4	1.46	0.31	0
27	20.09644	-0.0790	0.077	-23.128	3.01	1.003	1.6	32.20	39.10	4.8	5.0	-0.42	-0.133	-1.00	1.110	2.543	0.8	0.40	0.32	0
28	180.40768	1.1980	0.082	-22.225	2.14	0.903	-2.6	10.41	9.42	4.7	9.2	2.29	-0.848	-0.85	-1.773	2.197	0.6	0.09	0.03	0
29	118.18416	45.9493	0.052	-22.167	2.05	0.963	2.3	6.06	5.78	4.5	4.8	-0.45	-0.042	-0.96	-0.144	2.336	0.7	0.23	0.17	0
30	168.84945	54.4441	0.070	-22.802	1.99	0.939	2.6	7.22	7.38	6.3	5.6	-0.89	-0.041	-1.42	-1.795	2.349	1.0	0.09	0.25	2
31	232.31104	52.8640	0.073	-22.927	2.17	0.995	3.2	21.23	24.43	9.8	8.6	-0.34	0.017	-0.36	0.602	2.454	0.8	0.60	0.41	2
32	122.59694	42.2739	0.064	-22.719	2.40	1.013	3.7	4.56	5.02	2.4	2.9	0.10	-0.321	-1.31	1.298	2.571	0.9	0.63	0.21	2
33	184.62019	42.4610	0.073	-22.029	1.93	0.925	-0.4	9.19	9.73	5.1	4.6	-0.05	-0.054	-1.23	-1.015	2.284	0.9	0.15	0.17	2
34	254.08789	39.2752	0.062	-22.595	2.42	0.976	3.2	294.65	50.08	10.7	10.1	-1.20	-0.700	-1.01	-0.038	2.422	0.6	0.48	0.31	2
35	129.46447	26.5988	0.088	-22.705	1.88	0.903	2.2	6.32	8.82	6.2	6.3	-0.39	-0.069	-0.99	-2.875	2.413	0.5	0.92	0.09	2
36	134.49123	30.3439	0.086	-22.817	2.26	0.949	1.2	15.11	14.76	7.4	6.5	-0.10	-0.147	-0.57	-1.422	2.439	0.9	0.11	0.41	2
37	133.51888	29.0535	0.084	-22.938	2.50	1.002	4.6	8.06	13.29	2.9	3.6	1.72	-0.099	-0.49	0.964	2.463	0.9	0.35	0.36	2
38	237.97868	27.8640	0.082	-21.860	1.81	0.979	2.8	8.80	13.18	2.9	4.1	-0.01	-0.327	0.29	0.421	1.996	0.7	0.56	0.29	2
39	136.68638	3.6002	0.072	-22.123	1.90	0.893	-1.5	12.94	21.63	10.9	10.2	0.97	0.146	-0.51	-1.928	2.209	0.5	-0.07	0.05	2
40	144.40096	7.9180	0.093	-21.778	1.75	0.925	-1.3	2.70	4.25	4.2	4.4	0.91	-0.050	-1.40	-0.824	2.270	0.5	0.20	0.45	2
41	141.65320	3.4606	0.088	-22.235	2.15	0.954	3.3	4.45	7.72	4.8	5.9	-0.06	-0.075	-1.24	-0.427	2.422	0.9	0.21	0.19	2
42	178.15655	3.4727	0.081	-22.771	2.22	0.964	3.0	5.71	9.31	1.6	2.9	0.41	-0.625	0.03	-0.665	2.417	0.8	0.54	0.50	2
43	7.36845	-0.2126	0.060	-22.322	1.85	0.981	5.3	4.82	4.83	2.7	2.5	0.47	0.019	-1.35	0.288	2.390	0.8	0.41	0.32	2
44	216.19754	2.6644	0.053	-22.400	1.95	0.961	3.4	7.04	6.69	4.5	4.5	1.04	-0.009	-0.90	-0.344	2.401	0.8	0.34	0.25	2
45	223.93717	-0.3062	0.083	-22.295	1.92	0.905	1.7	1.09	1.49	2.0	2.4	0.91	-0.369	-0.81	-1.818	2.440	0.8	0.24	0.20	2
46	350.73485	-10.0456	0.084	-22.368	2.24	0.989	5.6	4.94	10.10	5.6	7.8	1.13	0.015	-1.10	0.477	2.444	0.9	0.32	0.36	2

Funding for the SDSS and SDSS-II has been provided by the Alfred P. Sloan Foundation, the Participating Institutions, the National Science Foundation, the U.S. Department of Energy, the National Aeronautics and Space Administration, the Japanese Monbukagakusho, the Max Planck Society, and the Higher Education Funding Council for England. The SDSS is managed by the Astrophysical Research Consortium for the Participating Institutions. The Participating Institutions are the American Museum of Natural History, Astrophysical Institute Potsdam, University of Basel, Cambridge University, Case Western Reserve University, University of Chicago, Drexel University, Fermilab, the Institute for Advanced Study, the Japan Participation Group, Johns Hopkins University, the Joint Institute for Nuclear Astrophysics, the Kavli Institute for Particle Astrophysics and Cosmology, the Korean Scientist Group,

the Chinese Academy of Sciences (LAMOST), Los Alamos National Laboratory, the Max-Planck-Institute for Astronomy (MPA), the Max-Planck-Institute for Astrophysics (MPIA), New Mexico State University, Ohio State University, University of Pittsburgh, University of Portsmouth, Princeton University, the United States Naval Observatory, and the University of Washington.

APPENDIX A

LIST OF PROPERTIES OF FGS AND FIELD GALAXIES

Table 2 lists all the quantities used to characterize the samples of FGs and field galaxies. FGs with extended X-ray contours ($N = 25$) have flag = 1 in Column 21, while field galaxies ($N = 17$) have flag = 2. The table also lists the four FG

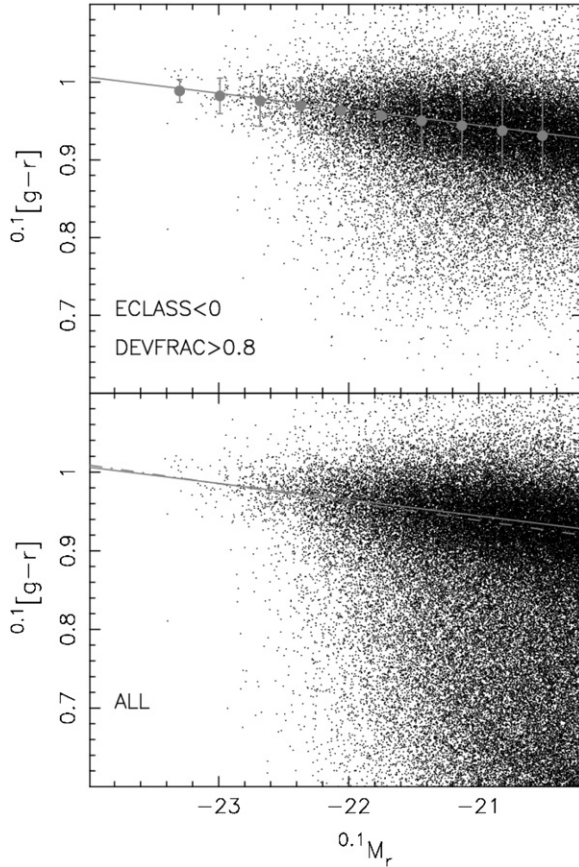


Figure 15. Color–magnitude diagram of early-type galaxies (the upper panel) and of all galaxies (the lower panel) in the catalog. The gray line in the upper panel shows the bi-weight fit to the data, while gray circles, and error bars plot the mean and standard deviation, σ_{g-r} , of the color distribution in different magnitude bins. The gray solid line in the lower panel is the same as that in the upper panel, while the gray dotted line shows the bi-weight fit to the color–magnitude relation of all galaxies in the catalog.

candidates that are not in the final FG sample because they do not fulfill the X-ray extension criterion. These objects have flag = 0. Column 1 is a running number for the list of FGs and field galaxies. Columns 2–4 give the R.A. and decl. (in degrees) and spectroscopic redshift from the SDSS DR4. Columns 5–7 provide the $z = 0.1$ k -corrected absolute magnitude, the magnitude gap of the FG, and the $g - r$ color, respectively. For field galaxies, the values of ΔM have been randomly assigned as described in Section 4. Column 8 provides the density excess around each galaxy. Columns 9 and 10 report the effective radii (in arcsec) in the g and r bands, while Columns 11 and 12 list the corresponding Sersic indices. Columns 13 and 14 provide the a_4 ($\times 100$) parameters and internal color gradients (in mag dex^{-1}). Column 15 reports the X-ray luminosity in units of $10^{44} h_{75}^{-2} \text{ erg s}^{-1}$. Column 16 provides the distance of each galaxy to the red sequence (Equation (3)). Columns 17 to 20 provide the velocity dispersions (in units of km s^{-1}) and stellar population parameters.

APPENDIX B

MEASURING THE RED SEQUENCE

To quantify the properties of the FG first-rank galaxies relative to the red sequence, we use the SDSS-DR4 galaxy catalog to calculate the offset, slope, and scatter of the $g - r$ versus r color–magnitude relation for all early-type galaxies. Following

a procedure similar to that of Bernardi et al. (2003), we select early-type galaxies on the basis of the SDSS spectroscopic parameter *eclass*, which classifies the spectral type using a principal component analysis, and the photometric parameter *fracDev_r*, which measures the fraction of the galaxy light distribution that is better fit by a de Vaucouleurs law. We define as early-type galaxies those systems with *eclass* < 0 and *fracDev_r* > 0.8, resulting in a sample of 39,733 (out of 91,563) galaxies selected from the SDSS catalog used to search for fossil systems (see Section 2.1). Total galaxy magnitudes are taken from the r -band Petrosian magnitudes output by the SDSS photometric pipeline, since they are model independent and highly reliable for bright galaxies. Colors are obtained from the g - and r -band SDSS model magnitudes because they are measured in the same aperture for all filters. Both magnitudes and colors are k -corrected using the *kcorrect* version 4_1_4 software package (Blanton et al. 2003), allowing k -corrections to be estimated through filters that are blueshifted by a factor $(1 + z_0)$. This procedure has the primary advantage of minimizing uncertainties on k -corrections, provided that the value of z_0 is close to the redshift range of the observed galaxies. Following other papers that analyze the color and magnitude distribution of galaxies in the SDSS database (e.g., Hogg et al. 2004), we choose $z_0 = 0.1$, corresponding to the upper redshift limit of our galaxy catalog, and we indicate the $z_0 = 0.1$ k -corrected model magnitudes with $^{0.1}g$ and $^{0.1}r$, and the $z_0 = 0.1$ k -corrected Petrosian absolute magnitude with the notation $^{0.1}M_r$.

Figure 15 shows the color–magnitude diagram of both early-type and all galaxies in our catalog. Although the catalog is almost complete down to $M_r = -20$ (see Section 2.1), we note that the difference in k -corrections for galaxies with $M_r \sim -20$ makes¹³ the color–magnitude diagram incomplete down to that magnitude limit. Therefore, we derive the slope, a , and the offset, b , of the color–magnitude relation by minimizing the rms of galaxy colors around the linear relation, using only galaxies brighter than $M_r \sim -20.2$. To reduce the effect of outliers, color rms is computed via bi-weight statistics (Beers et al. 1990). The uncertainties on a and b are estimated through the bootstrap method, with $N = 1000$ bootstrap iterations. For the sample of early-type galaxies, we find $a = 0.944 \pm 0.005$ and $b = -0.0206 \pm 0.003$, consistent with $b = -0.022$ reported by Hogg et al. (2003) and with other results in the literature (e.g., Cool et al. 2006; Gallazzi et al. 2006). The derived values of a and b change by less than 10% if we apply the same fitting procedure to the entire galaxy catalog (i.e., not applying the *eclass* and *fracDev_r* cuts), demonstrating the robustness of the regression method. To estimate the scatter around the color–magnitude relation, we bin the sample of early-type galaxies with respect to magnitude, and derive the color rms, σ_{g-r} , in each bin with bi-weight statistics. Figure 16 plots σ_{g-r} as a function of $^{0.1}M_r$. We find that σ_{g-r} increases at the faintest magnitudes, with this trend well fit by the relation

$$\sigma_{g-r}(^{0.1}M_r) = 0.045 - 0.00047 \times (^{0.1}M_r + 20.2)^4, \quad (\text{B1})$$

in the magnitude range $-23 < ^{0.1}M_r < -20.2$. The mean value of σ_{g-r} is 0.035, consistent with that found in previous studies (see e.g., Cool et al. 2006).

¹³ As mentioned in Section 5, k -corrections have not been applied when computing total magnitudes to select the SDSS-DR4 catalog.

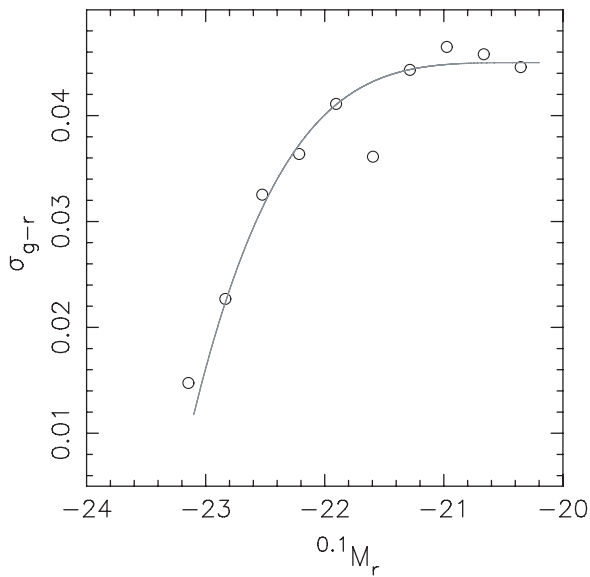


Figure 16. Scatter around the red sequence, σ_{g-r} , plotted as a function of central value of each magnitude bin in the upper panel of Figure 15. The gray curve is the polynomial fit to the points, as given in Equation (B1).

APPENDIX C

MEASURING STRUCTURAL PARAMETERS AND INTERNAL COLOR GRADIENTS

Structural parameters were derived using 2DPHOT (La Barbera et al. 2008, hereafter LdC08), an automated software environment that performs several tasks, such as catalog extraction (using SExtractor; Bertin & Arnouts 1996), star/galaxy separation, and surface photometry. To estimate color gradients, structural parameters were measured in both the g and r bands. For each galaxy in the FG and field (FS) samples we retrieved the corresponding g - and r -band *corrected frames* from the SDSS DR4 Data Archive Server and ran 2DPHOT on them. A complete description of the 2DPHOT package can be found in LdC08; here we provide a brief description of the steps relevant to measuring galaxy structural parameters. For each galaxy, a PSF model was constructed by fitting the four closest stars in the image with a sum of three two-dimensional Moffat functions. Isophotal distortions of star isophotes were modeled as described in LdC08. The parameters r_e , $\langle \mu \rangle_e$ and n were then obtained by fitting galaxy images with PSF-convolved Sersic models. As an example of the fitting procedure, Figure 17 plots the images of a subset of galaxies from the list of 25 FGs, along with the residuals after subtracting the best-fitting Sersic models. The shapes of FG and FS candidates are characterized by the isophotal shape parameter, a_4 , of each galaxy. Isophotal contours were expanded into a \sin/\cos series (Bender & Möllenhoff 1987), and analyzed as described in LdC08, by deriving the a_4 coefficient as the average of the a_4 profile within a radial range from 4 times the FWHM to twice the galaxy effective radius.

Internal color gradients, defined as the logarithmic slope of the galaxy radial color profile, were estimated as follows (see also La Barbera et al. 2003). For each galaxy in the FG and FS samples, the corresponding g - and r -band best-fitting Sersic parameters were used to construct seeing-deconvolved galaxy images. A set of concentric ellipses were constructed for both the g - and r -band galaxy images, with all ellipses having the same position angle and axis ratio parameters as those derived from the r -band Sersic fitting (Appendix C). For each ellipse, a $g-r$ color was calculated as the average ratio of the g -

and r -band intensity values along that ellipse. The color profile was then computed as the average $g-r$ color as a function of the equivalent radius of the corresponding ellipse. An ordinary least-squares fit to the color profile, adopting the color index as the independent variable, was then performed, with the slope of the fitted line yielding the internal color gradient for each galaxy. Following previous studies of color gradients in early-type galaxies (e.g., Peletier et al. 1990), the fit was performed in a range of the color profile, from an inner radius of 0.1 to an outer radius of 1.0 times the r -band effective radius.

APPENDIX D

SPECTRAL ANALYSIS

D.1. Measuring Spectral Parameters

The spectra of FGs and field galaxies were masked to avoid bad pixels affecting the wavelength ranges defining the spectral indices, brought to redshift zero and corrected for foreground dust extinction following Schlegel et al. (1998). Then, we derived the spectral indices $H\beta$, $[MgFe]' = (Mgb(0.72 \times Fe5270 + 0.28 \times Fe5335))^{1/2}$, $Fe3 = (Fe4383 + Fe5270 + Fe5335)/3$, and $\langle Fe \rangle = (Fe5270 + Fe5335)/2$, which are defined according to the Lick system (Worthey & Ottaviani 1997; González 1993), except for the higher resolution of the SDSS spectra.

The measurement of the $H\beta$ spectral index, which is directly related to age, may be significantly affected by nebular emission, biasing the inferred age toward older values. To correct for this effect, we used the STARLIGHT code (Cid Fernandes et al. 2005) which finds the best fit to the observed spectrum by combining a set of SSP-MILES SEDs (see Section 8), convolved to the SDSS spectral resolution and broadened to match the galaxy's velocity dispersion. As a result of the fitting procedure, STARLIGHT also provides the velocity dispersion, σ , of each galaxy. During the fitting process, regions around emission lines were masked. Figure 18 shows how the residual spectrum unveils the nebular emission. Instead of correcting for the residual emission line, we measured the $H\beta$ index directly from the absorption spectra obtained by STARLIGHT.

Velocity dispersions of FGs and field galaxies were taken from the SDSS DR4. For 53 galaxies (out of 102 FG candidates and 66 field galaxies with significant X-ray detection), the σ measurements were not available from the SDSS database, and in this case we adopted the STARLIGHT estimates. The spectral parameters, i.e., velocity dispersions and spectral indices, were corrected to a common physical aperture of $R_{\text{eff}}/8$, following Jørgensen et al. (1995) and Jørgensen (1997). For each galaxy, the effective radius, R_{eff} , was defined as $R_{\text{eff}} = (b/a) \times R_{\text{dev}}$, using the $deV Rad_r$ (R_{dev}) and $deVAB_r$ (b/a) parameters from the SDSS database. Since the aperture corrections rely on effective radii derived by fitting de Vaucouleurs models, we adopted the SDSS photometric pipeline's R_{eff} values, instead of using our effective radii derived using Sersic models (see Appendix C).

D.2. Extraction of Stellar Population Parameters

We measured age, metallicity and abundance ratio $[\alpha/Fe]$ using the recently developed α -enhanced SSP-MILES models (I. G. de la Rosa et al. 2008, in preparation), which provide SEDs at 2.4 Å (FWHM) resolution for different α -enhancement ratios, combining theoretical (Coelho et al. 2005) and empirical (MILES) libraries (Sánchez-Blázquez et al. 2006). For each galaxy, we constructed a grid of $H\beta$ and $[MgFe]'$ values using

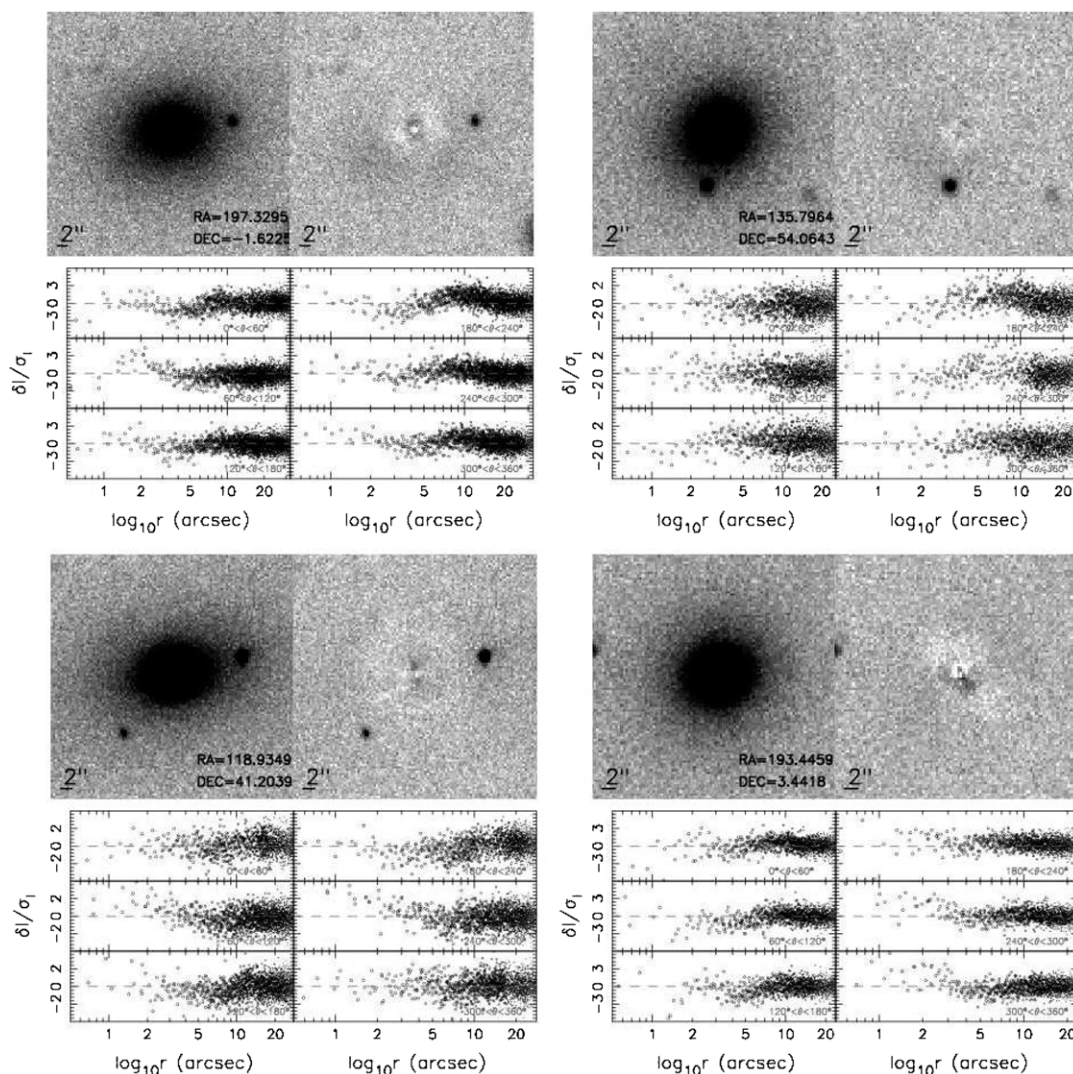


Figure 17. Two-dimensional fitting of four galaxies drawn from the sample of 25 FGs. For each galaxy, the upper left and upper right subpanels show the galaxy *r*-band image and the corresponding residual map after model subtraction, respectively. Right ascension and declination are reported, in degrees, in the lower right corner of the left subpanel. The spatial scale is shown in the lower left corners. The lower six subpanels show the fitting residuals, normalized to the photon noise in each pixel, as a function of the radial distance, *r*, to the galaxy center within six bins of the polar angle, θ , respectively. The limits of each bin are shown in the lower right corner of each subpanel.

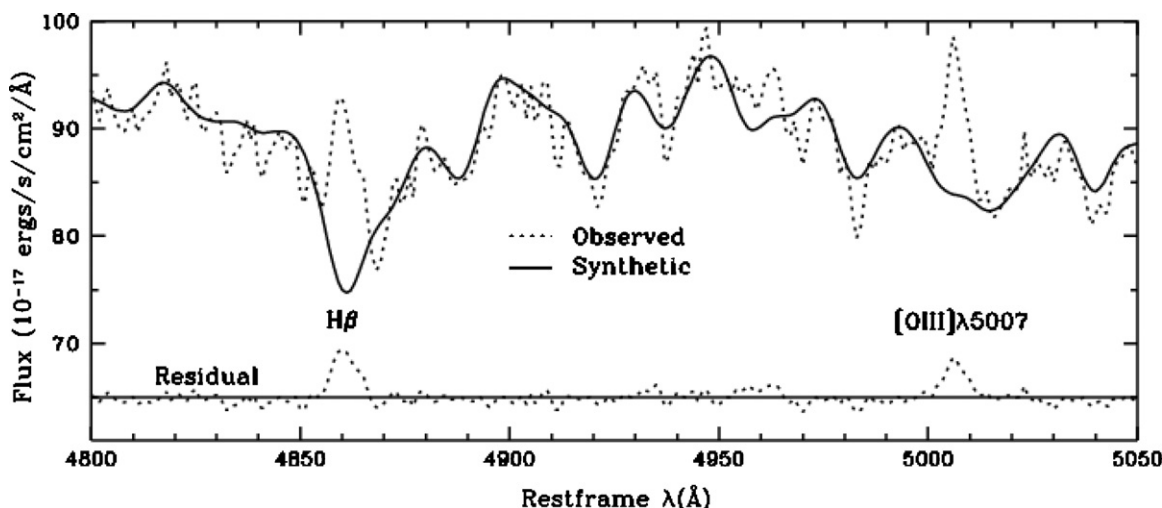


Figure 18. Synthetic spectrum obtained by STARLIGHT (continuous line) is the combination of SSP models which best fits the observed SDSS spectrum (dotted line). The residual spectrum (observed–synthetic), can be used to measure emission indices. Instead of correcting for emission filling, we measure the $H\beta$ index directly from the synthetic spectrum.

the solar metallicity SSP models ($[\alpha/\text{Fe}] = 0$) with a variety of age and $[Z/H]$ combinations. The age and $[Z/H]$ of the observed spectrum were obtained by interpolating its two spectral indices among those of the models. The $H\beta$ and $[\text{MgFe}]'$ indices are mostly sensitive to age and metallicity, respectively, breaking the well-known age–metallicity degeneracy. Moreover, they have the advantage of being almost insensitive to $[\alpha/\text{Fe}]$ (Korn et al. 2005). As a second step, after fixing the estimated age, we construct a new grid of Fe3 and Mgb values with models having a variety of $[Z/H]$ and $[\alpha/\text{Fe}]$ combinations. Interpolation of the observed indices yields the final metallicity and $[\alpha/\text{Fe}]$ values. To check the reliability of the α -enhancement estimates, we repeated the above computation, replacing the Fe3 index with $\langle \text{Fe} \rangle = (\text{Fe}5270 + \text{Fe}5335)/2$. The two procedures are fully consistent at a confidence level of 2σ for all but three of the FG and FS galaxies. For those three objects, we adopted the more accurate $\langle \text{Fe} \rangle$ estimate (see I. G. de la Rosa et al. 2008, in preparation).

REFERENCES

- Adami, C., et al. 1998, *A&A*, **336**, 63
 Anderson, S. F., et al. 2007, *AJ*, **133**, 313
 Avni, Y., & Bahcall, J. N. 1980, *ApJ*, **235**, 694
 Bajaja, E., et al. 2005, *A&A*, **440**, 767
 Barnes, J. E. 1989, *Nature*, **338**, 123
 Beers, T. C., Flynn, K., & Gebhardt, K. 1990, *AJ*, **100**, 32
 Bender, R., & Möllenhoff, C. 1987, *A&A*, **177**, 71
 Bernardi, M., et al. 2003, *AJ*, **125**, 1817
 Bertin, E., & Arnouts, S. 1996, *A&AS*, **117**, 393
 Beuing, J., et al. 1999, *MNRAS*, **302**, 209
 Blanton, M. R., et al. 2003, *AJ*, **125**, 2276
 Blanton, M. R., et al. 2005, *ApJ*, **629**, 143
 Böhringer, H., et al. 2000, *ApJS*, **129**, 435
 Cid Fernandes, R., et al. 2005, *MNRAS*, **358**, 363
 Coelho, P., et al. 2005, *A&A*, **443**, 735
 Cool, R. J., et al. 2006, *AJ*, **131**, 736
 Dariush, A., et al. 2007, *MNRAS*, **382**, 433
 de Grandi, S., et al. 1997, *ApJ*, **486**, 738
 de la Rosa, I. G., et al. 2007, *AJ*, **133**, 330
 D'Onghia, E. D., et al. 2005, *ApJ*, **630**, L109
 Evrard, A. E., et al. 1996, *ApJ*, **469**, 494
 Gal, R. R., et al. 2003, *AJ*, **125**, 2064
 Gallazzi, A., et al. 2006, *MNRAS*, **370**, 1106
 Gómez, P. L., et al. 2003, *ApJ*, **584**, 210
 González, J. J. 1993, PhD thesis, Univ. California Santa Cruz
 Hausman, M. A., & Ostriker, J. P. 1978, *ApJ*, **224**, 320
 Hogg, D. W., et al. 2003, *ApJ*, **585**, 5
 Hogg, D. W., et al. 2004, *ApJ*, **601**, 29
 Jones, L. R., et al. 2000, *MNRAS*, **312**, 139
 Jones, L. R., et al. 2003, *MNRAS*, **343**, 627
 Jørgensen, I. 1997, *MNRAS*, **288**, 161
 Jørgensen, I., Franx, M., & Kjaergaard, P. 1995, *MNRAS*, **276**, 1341
 Kewley, L. J., et al. 2006, *MNRAS*, **372**, 961
 Khosroshahi, H. G., Jones, L. R., & Ponman, T. J. 2004, *MNRAS*, **349**, 1240
 Khosroshahi, H. G., Ponman, T. J., & Jones, L. R. 2006, *MNRAS*, **372**, 68
 Khosroshahi, H. G., Ponman, T. J., & Jones, L. R. 2007, *MNRAS*, **377**, 595
 Kobayashi, C. 2005, *MNRAS*, **361**, 1216
 Kodama, T., et al. 1998, *A&A*, **334**, 99
 Komossa, S., Böhringer, H., & Huchra, J. P. 1999, *A&A*, **349**, 88
 Korn, A. J., Maraston, C., & Thomas, D. 2005, *A&A*, **438**, 685
 La Barbera, F., et al. 2003, *A&A*, **409**, 21
 La Barbera, F., et al. 2005, *ApJ*, **626**, 19L
 La Barbera, F., et al. 2008, *PASP*, **120**, 681
 Lee, H., et al. 2006, *ApJ*, **647**, L970
 McCarthy, P. J., et al. 2004, *ApJ*, **614**, 9
 Mulchaey, J. S., & Zabludoff, A. I. 1999, *ApJ*, **514**, 133
 Peletier, R. F., et al. 1990, *AJ*, **100**, 1091
 Ponman, T. J., & Bertram, D. 1993, *Nature*, **363**, 51
 Ponman, T. J., et al. 1994, *Nature*, **369**, 462
 Proctor, R. N., et al. 2004, *MNRAS*, **349**, 1381
 Raymond, J. C., & Smith, B. W. 1977, *ApJS*, **35**, 419
 Romer, A. K., et al. 2000, *ApJS*, **126**, 209
 Sánchez-Balazquez, P., et al. 2006, *MNRAS*, **371**, 703
 Santos, W. A., Mendes de Oliveira, C., & Sodr , L. J. 2007, *AJ*, **134**, 1551
 Schlegel, D., Finkbeiner, D. P., & Davis, M. 1998, *ApJ*, **500**, 525 (SFD98)
 Sorrentino, G., Antonuccio-Delogu, V., & Rifatto, A. 2006, *A&A*, **460**, 673
 Sthoughton, C., et al. 2002, *AJ*, **123**, 485
 Sun, M., et al. 2004, *ApJ*, **612**, 805
 Tozzi, P., et al. 2006, *A&A*, **451**, 457
 Ulmer, M. P., et al. 2005, *ApJ*, **624**, 124
 Vikhlinin, A., et al. 1999, *ApJ*, **520**, 1
 Voges, W., et al. 1999, *A&A*, **349**, 389
 Worthey, G., & Ottaviani, D. L. 1997, *ApJS*, **111**, 377
 Wu, H., et al. 2005, *ApJ*, **622**, 244
 Yoshioka, T., et al. 2004, *AdSpR*, **34**, 2525